



Observational perspective on sudden stratospheric warmings and blocking from Eliassen–Palm fluxes

Kamilya Yessimbet^{1,2}, Andrea K. Steiner^{1,2}, Florian Ladstädter¹, and Albert Ossó¹

¹Wegener Center for Climate and Global Change, University of Graz, 8010 Graz, Austria

²FWF-DK Climate Change, University of Graz, 8010 Graz, Austria

Correspondence: Kamilya Yessimbet (kamilya.yessimbet@uni-graz.at)

Received: 4 December 2023 – Discussion started: 25 January 2024

Revised: 31 May 2024 – Accepted: 13 July 2024 – Published: 27 September 2024

Abstract. In this study, we examine eight major boreal sudden stratospheric warming (SSW) events between 2007 and 2019 to understand the vertical coupling between the troposphere and stratosphere as well as the relationship between SSWs and blocking events using global navigation satellite system (GNSS) radio occultation (RO) observations. Our study covers the main aspects of SSW events, including the vertical structure of planetary-wave propagation, static stability, geometry of the polar vortex, and occurrence of blocking events. To analyze wave activity and atmospheric circulation, we compute the quasi-geostrophic Eliassen–Palm (EP) flux and geostrophic winds. The results show that the observations agree with theory and previous studies in terms of the primary dynamic features and provide a detailed view of their vertical structure. We observe a clear positive peak of upward EP flux in the stratosphere prior to all SSW events. In seven out of eight events, this peak is preceded by a clear peak in the troposphere. Within the observed timeframe, we identify two types of downward dynamic interactions and the emergence of blocking events. During the 2007 and 2008 “reflecting” events, we observe a displacement of the polar vortex along with a downward propagation of wave activity from the stratosphere to the troposphere during vortex recovery, coinciding with the formation of blocking in the North Pacific region. Conversely, in the other six SSW “absorbing” events from 2009 to 2019, which were characterized by a vortex split, we observe wave absorption and the subsequent formation of blocking in the Euro-Atlantic region. The analysis of the static stability demonstrates an enhancement of the polar tropopause inversion layer as the result of SSWs, which was stronger for the absorbing events. Overall, our study provides an observational view of the synoptic and dynamic evolution of the major SSWs, their link to blocking, and the impact on the polar tropopause.

1 Introduction

In winter, dynamical coupling between the troposphere and stratosphere, in particular the stratospheric polar vortex (SPV), is an important source of surface climate variability. The coupling is mediated by wave–mean flow interactions and often occurs via the downward progression of zonal-mean anomalies following large SPV anomalies (Baldwin and Dunkerton, 2001). These downward anomalies can induce a change in the tropospheric circulation with patterns that resemble the annular modes (Baldwin and Dunkerton, 1999, 2001). In another view, the downward influence is

mediated by the reflection of planetary wave activity from the stratosphere into the troposphere (Hines, 1974; Geller and Alpert, 1980; Perlwitz and Harnik, 2004; Matthias and Kretschmer, 2020; Messori et al., 2022).

In this study, we focus on connections between sudden stratospheric warming (SSW) events, i.e., extreme cases of SPV variability, and atmospheric blocking, i.e., persistent high-pressure systems that interrupt the regular westerly flow at midlatitudes. We adopt two distinctive classifications for SSWs. Depending on the SPV geometry, the first classification categorizes them into displacement and split events. In the displacement type of SSWs, the polar vortex is dis-

placed away from the pole, and in the split type, the polar vortex breaks up into daughter vortices (Butler et al., 2017). The second classification divides SSWs into reflecting and absorbing events based on the planetary-wave activity evolution (Kodera et al., 2016). Reflecting SSW events are characterized by the downward reflection of planetary waves from the stratosphere into the troposphere, whereas absorbing events indicate non-reflecting stratospheric conditions, implying wave absorption by the stratosphere, during SSW recovery. While the former classification describes the SPV behavior during the mature phase of SSWs, the latter describes the behavior of planetary-wave activity during the recovery phase of SSWs, with a more pronounced focus on their impact on the troposphere.

In terms of the impacts on the troposphere, reflecting SSW events have been linked to the occurrence of North Pacific blocking, while absorbing SSWs have been associated with a hemispheric near-surface pattern of relatively high pressure over the polar region and low pressure in the midlatitudes that resembles the negative phase of the Arctic Oscillation (AO) (Kodera et al., 2016). Some studies have suggested that the split and displacement types of SSW events may also lead to different tropospheric responses (Mitchell et al., 2013). However, other studies, such as Maycock and Hitchcock (2015), have not found significant differences in the tropospheric impacts of the split and displacement events.

The atmospheric layer where the main dynamic coupling occurs is the upper troposphere and lower stratosphere (UTLS). An accurate representation of the vertical structure of the UTLS is known to be important for the resolution of atmospheric dynamics and circulation in coupled climate models (Gerber and Manzini, 2016). This, in part, underpins the rationale for employing global navigation satellite system (GNSS) radio occultation (RO) data – which are known for their stability, accuracy, and high vertical resolution within the UTLS (Steiner et al., 2020) – in our study. There have been previous studies resolving important aspects of atmospheric dynamics from RO data, such as Leroy and Anderson (2007), in which the quasi-geostrophic Eliassen–Palm (EP) flux was calculated; Scherllin-Pirscher et al. (2014) and Verkhoglyadova et al. (2014), in which geostrophic winds were calculated; Healy et al. (2020), in which quasi-biennial oscillation (QBO) zonal winds were retrieved; and Pilch Kedzierski et al. (2020), in which Rossby waves were studied.

In this study, we utilize globally distributed direct measurements of geopotential height and temperature fields from RO data. These measurements are used to compute geostrophic winds, the blocking index, the quasi-geostrophic EP flux, and the static stability. The computed parameters are then used as a basis for our synoptic and dynamic analysis of SSW events that occurred between 2007 and 2019. Our main objective is to characterize the dynamics induced by these SSW events and examine their links to blocking events from an observational perspective. We focus on the analysis of the

vertical aspects of the EP flux, as it plays a critical role in understanding how the stratospheric circulation responds to the upward propagation of planetary-wave activity from the troposphere (Yessimbet et al., 2022a). Due to its high vertical resolution, RO is shown in this study to be particularly suitable for providing information for the dynamic and synoptic analysis of SSW events and blocking events (e.g., Brunner et al., 2016).

We describe the RO dataset and detail the methods employed in Sects. 2 and 3, respectively. Section 4 presents the results for all investigated SSW events from 2006 to 2019 with a detailed analysis of two representative SSW events in February 2008 and January 2019. Finally, we discuss and draw conclusions about our findings in Sect. 5.

2 Data

This study employs measurements from GNSS RO collected by various satellite missions, including CHAMP (Wickert et al., 2001), SAC-C (Hajj et al., 2004), GRACE (Beyerle et al., 2005; Wickert et al., 2005), MetOp (Luntama et al., 2008), and Formosat-3/COSMIC (Anthes, 2011). The GNSS RO method is based on the detection of radio signals transmitted by GNSS satellites, which are refracted by the Earth's atmosphere as they propagate through it to low Earth orbit (LEO) satellites. The measured signal phase changes are converted to bending angle profiles and further to refractivity by an Abel transform. At high altitudes, the Abel integral requires initialization with background data. Thermodynamic parameters are then computed under the assumption of a dry atmosphere (“dry” parameters). In moist air conditions (lower to middle troposphere, specifically in the tropics), the retrieval of the (physical) temperature or humidity requires prior knowledge of the state of the atmosphere (e.g., Kursinski et al., 1995, 1996; Healy and Eyre, 2000). Due to the background data involved, the retrieved RO temperature data exhibit larger uncertainties in the lowermost moist parts of the troposphere and at high altitudes (above about 30 km). For an overview of the retrieval process and the structural uncertainties involved, see, e.g., Steiner et al. (2011, 2020). The RO measurements are of high quality, with minimal structural uncertainty within the UTLS region, as highlighted by Scherllin-Pirscher et al. (2017) and Steiner et al. (2020).

In this work, we use the geopotential height and physical temperature as a function of pressure, as processed by the Wegener Center for Climate and Global Change (WEGC) with the Occultation Processing System (OPS) version 5.6 (Angerer et al., 2017; Steiner et al., 2020) using the phase delay data derived at the University Corporation for Atmospheric Research COSMIC Data Analysis and Archive Center (UCAR/CDAAC).

Geostrophic-wind fields can be derived from RO geopotential-height fields (Scherllin-Pirscher et al., 2014, 2017). RO geostrophic-wind and gradient-wind fields were

found to capture all the main wind features in our study. Compared to atmospheric analyses, wind differences are generally small (2 m s^{-1}) except near the subtropical jet (up to 10 m s^{-1}). There, RO winds underestimate the actual winds due to the geostrophic- and gradient-wind approximations, while RO retrieval errors have negligible effects (Scherllin-Pirscher et al., 2014).

The number of daily RO profiles retrieved from different missions varied over the period from 2006 to 2019, with the highest number of profiles occurring from 2007 to 2010 (> 2500 profiles per day) and the number of profiles decreasing (from more than 2500 to less than 2000 profiles) from 2012 onwards (Fig. S1 in the Supplement) as the lifetimes of some of the RO missions were exceeded (Fig. 5; Angerer et al., 2017).

Utilizing data from the available records spanning 2006 to 2019, we focus on the daily wintertime period from November to March. The vertical grid consists of 147 pressure levels from 1000 to 10 hPa (the levels are 200 m apart – i.e., equidistant in altitude space – up to 20 km and 500 m apart above that). To generate $2.5^\circ \times 2.5^\circ$ gridded bins from the profile data, we employ a spatial and temporal weighting methodology. This involves applying Gaussian weighting according to the latitude–longitude distances of each profile in relation to the bin center, taking all profiles within 600 km from the center into account. An additional temporal Gaussian weighting of $\pm 2 \text{ d}$ around the given day is also applied. With this, we reduce the number of missing grid points while maintaining as much measurement information as possible. Thus, in the range of vertical pressure levels from 10 to 850 hPa, there are fewer than 10 missing grid points in the daily gridded fields, with the number increasing towards the surface. For any remaining missing grid points, we use bilinear interpolation to fill in these gaps.

3 Method

This study applies a geostrophic approximation to derive winds directly from geopotential heights, as it balances the pressure gradient with Coriolis forces. RO measurements allow the retrieval of geopotential height as an independent vertical coordinate. The computation of geostrophic winds is based on Scherllin-Pirscher et al. (2014).

To study wave activity, we calculate the quasi-geostrophic EP flux based on Edmon et al. (1980). According to the definition of the EP flux for spherical geometry, the meridional F_ϕ and vertical F_p components are defined as

$$\mathbf{F} = (F_\phi, F_p) = a \cos \phi \left(-\overline{u'v'}, f \frac{\overline{v'\theta'}}{\frac{\partial \theta}{\partial p}} \right), \quad (1)$$

where a denotes the equatorial radius of the Earth, p denotes the logarithm of the pressure, ϕ is the latitude, and θ is the potential temperature. The Coriolis parameter f equals

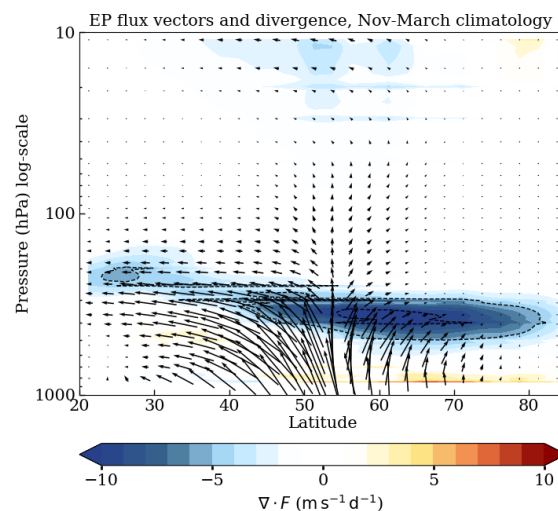


Figure 1. Climatological Eliassen–Palm flux vectors and divergence (shading) for November to March from 2006 to 2019. The vectors are plotted for every fifth pressure level.

$2\Omega \sin \phi$, where Ω is the Earth’s angular velocity, u and v are the geostrophic meridional and zonal winds, the overlines denote zonal averages, and primes indicate deviations from zonal averages. Divergence of the EP flux, $\nabla \cdot \mathbf{F} \equiv \frac{\partial F_\phi}{\partial \phi} + \frac{\partial F_p}{\partial p}$, scaled by $\frac{1}{a \cos \phi}$, indicates an acceleration of the zonal flow. The climatological EP flux for winter 2006 to 2019 is shown in Fig. 1, where a convergence zone (blue shading) with upward-directed EP flux vectors is observed in the upper troposphere, which means that the wave activity is intensified in the wintertime upper troposphere. For display purposes, EP flux vectors are scaled as follows:

$$(\mathbf{F}_\phi, \mathbf{F}_p) = \cos \phi \left(\frac{F_\phi}{a\pi}, \frac{F_p}{10^5} \right), \quad (2)$$

according to commonly used methods (NOAA’s Physical Sciences Laboratory, 2023).

The 3D wave activity flux, the Plumb flux, presented in Appendix B, is computed according to Plumb (1985; Eq. 5.7). In addition, we also compute the eddy meridional heat flux $v'T'$ at 100 hPa and averaged over $45\text{--}75^\circ \text{ N}$, similar to Kodera et al. (2016), who used it as a proxy for the vertical wave propagation between the troposphere and the stratosphere to characterize reflecting and absorbing SSW events. The computation of anomalies is performed by subtracting the 2007–2019 daily mean climatology. A standard algorithm based on 500 hPa geopotential-height gradients and described in Brunner and Steiner (2017) and Brunner (2018) is used to calculate the blocking index. Two distinct blocking regions have been defined based on the highest frequencies of blocking during the wintertime: the North Pacific (160° E to 160° W) and Euro-Atlantic (30° W to 45° E).

To examine further effects of the different SSW types, we compute the static stability in the form of the Brunt–Väisälä

frequency, N^2 , defined as follows:

$$N^2 = -\frac{pg^2 \frac{\partial \theta}{\partial p}}{RT\theta}, \quad (3)$$

where g denotes the gravitational acceleration ($g = 9.81 \text{ m s}^{-2}$), R is the gas constant of dry air ($R = 287 \text{ J kg}^{-1} \text{ K}^{-1}$), and T is the temperature.

In our analysis, we also make comparisons of key parameters such as the zonally averaged parameters, zonal-mean zonal wind, and $\overline{v'T'}$ (Figs. S2 and S3) between RO and reanalyses (e.g., ERA5), which confirm the consistency and the reliability of the RO-based dynamics.

For the definition of major SSW events, we adopt a commonly used definition from Butler et al. (2017), which defines the central date of an SSW event as the day when the zonal-mean zonal wind at 10 hPa and 60° N , \bar{u} , changes from westerly to easterly. The diagnosed central SSWs are compared with the list of major midwinter SSWs in reanalysis products in the SSW Compendium dataset (NOAA CSL, 2024).

4 Results

Section 4.1 describes the commonalities in the key dynamics of the 2007 and 2008 winters. To illustrate this, we show the results of the analysis of the 2008 winter as a representative case study. Similarly, Sect. 4.2 presents the 2019 SSW event as an example to describe the commonalities between the 2009, 2010, 2013, 2016, and 2018 events. In Sect. 4.3, we analyze the vertical wave activity and static stability for all SSW events from 2007 to 2019.

4.1 Type I: SSW events in 2007 and 2008

One of the main commonalities of the 2008 and 2007 events was the SPV displacement. Figure 2a shows the vortex evolution during the main phases of the winter of 2008. During December and January, the vortex remained strong and symmetrically centered at the North Pole. In February, the vortex began to weaken, losing its symmetry and finally shifting from the pole towards Eurasia. The vortex weakening was marked by warming, with stratospheric polar-cap ($65\text{--}90^\circ \text{ N}$) temperature anomalies exceeding the climatological mean and showing short-term fluctuation (Fig. 3a, b). While the vortex was displaced, positive polar-cap temperature anomalies propagated downwards to around 70 hPa. On 22 February, \bar{u} turned easterly (Fig. 3c), marking the central date of a major SSW event. The reversal of \bar{u} lasted for 6 d, followed by a period of recovery and gradual cooling. A similar pattern was observed in the winter of 2007, with a vortex displacement and \bar{u} reversal on 24 February that lasted only 4 d and was also accompanied by fluctuating stratospheric polar-cap temperature anomalies (Figs. A1a, A2a, b).

Another common feature of the 2008 and 2007 SSW events was a relatively short (about 12 and 13 d) pulse of

wave activity propagation (responsible for the \bar{u} reversal) and its significant decrease (marked by a negative $\overline{v'T'}$) during the first week of the SSW recovery phase. The onset of the SSW recovery phase is defined as the date when the maximum North Pole ($80\text{--}90^\circ \text{ N}$) temperature anomalies at 50 hPa are reached (Kodera et al., 2016).

For the 2008 event, $\overline{v'T'}$ at 100 hPa and averaged across $45\text{--}75^\circ \text{ N}$ is shown in Fig. 3c. The behavior of $\overline{v'T'}$ is coherent with that of \bar{u} : as $\overline{v'T'}$ increases, indicating the upward propagation of planetary-wave activity, the wind speed decreases. From the beginning of February, a weakening of \bar{u} occurred concurrent with the occurrence of two consecutive $\overline{v'T'}$ peaks with a 2 d lag between them. The 2 d lag between these two pulses may be an indication that the upward wave activity was suppressed and then resumed. The reversal of \bar{u} occurred during the second $\overline{v'T'}$ peak, which lasted the 12 d from 15 to 26 February. In the first week of the SSW recovery phase, the $\overline{v'T'}$ was characterized by negative values.

The time–height representation of the vertical component of EP flux as a function of pressure F_p is shown in Fig. 3d. From 7 February, there was a negative F_p anomaly below 300 hPa, indicating an intensification of wave activity. Following this, a mildly negative F_p pattern was observed, first between 300 and 100 hPa and then above 20 hPa with a delay of 2 d. Another (less intense) negative F_p anomaly appeared below 400 hPa on 15 February and later extended to about 100 hPa, which indicates the upward propagation of wave activity. Between 18 February and the central date of the SSW event, a pronounced negative F_p anomaly was noticeable above 100 hPa. Following the central SSW date, a substantial positive F_p anomaly became apparent below 300 hPa before being succeeded by a minor positive F_p anomaly within the stratosphere. Starting from 29 February, the second peak of the positive F_p anomaly maximized below the 300 hPa level and extended throughout the entirety of the atmospheric column. These instances of positive F_p anomaly peaks were consistent with the negative $\overline{v'T'}$ peak observed from 27 February to 6 March, as illustrated in Fig. 3c. The negative $\overline{v'T'}$ peak suggests a substantial reduction in the propagation of planetary-wave activity into the stratosphere or a downward propagation of wave activity due to the reflection of these waves from the stratosphere into the troposphere.

The negative $\overline{v'T'}$ peak from 27 February to 6 March coincided with the occurrence of blocking in the North Pacific, as shown in Fig. 3e. Note that for the 2007 SSW event, there was also a negative $\overline{v'T'}$ peak concurrent with the development of North Pacific blocking (Fig. A2c, e). In Fig. 2b, the manifestation of North Pacific blocking is evident through a positive 500 hPa geopotential-height anomaly from 27 to 29 February. Notably, the arrangement of the 500 hPa geopotential-height anomaly field corresponded to that of the 50 hPa field. The barotropic low-pressure system over eastern Eurasia indicated a polar-vortex shift toward Eurasia. This

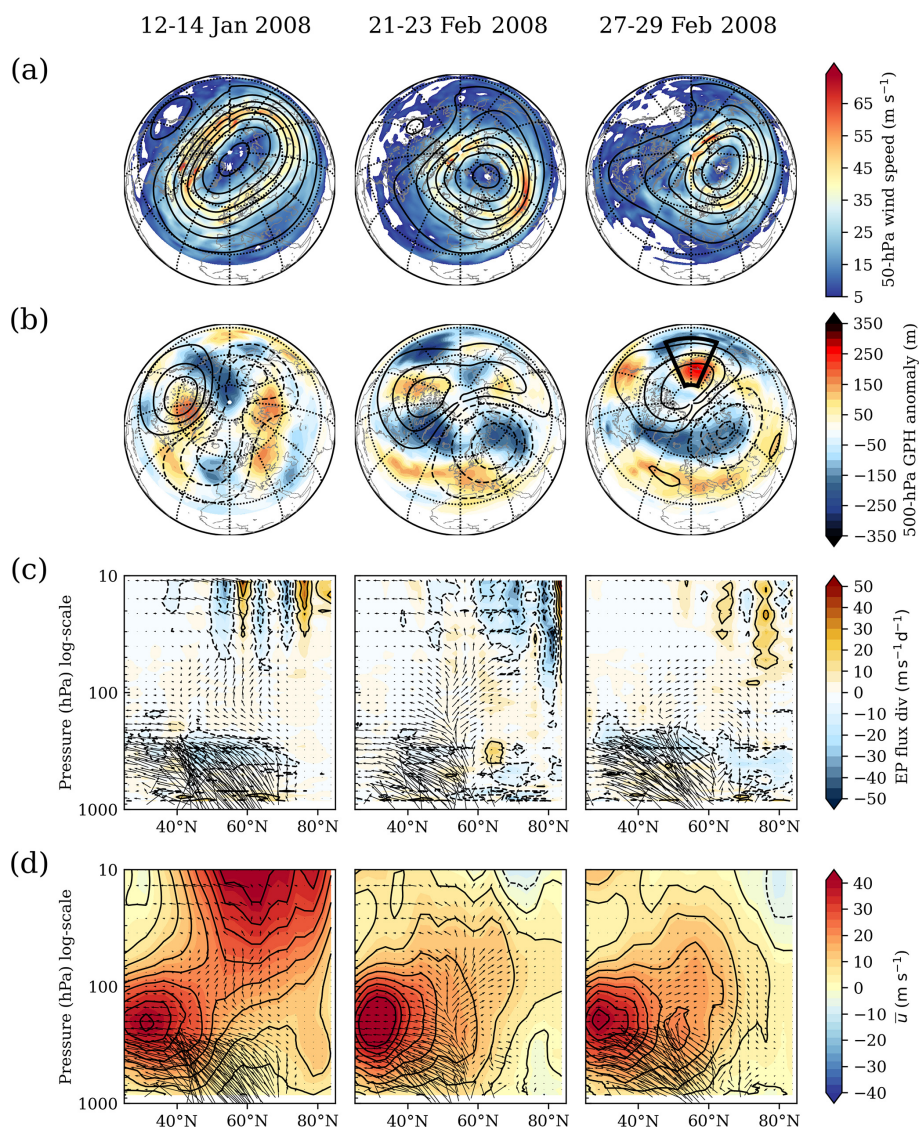


Figure 2. Evolution of the 2008 SSW, as shown by the results at three dates: before the SPV displacement (left), during its displacement (center), and during its recovery (right). **(a)** 50 hPa wind speed (shading) and 50 hPa geopotential height (contours). **(b)** 500 hPa geopotential-height anomaly (shading) and 50 hPa geopotential-height anomaly (contours). The black box indicates the North Pacific blocking region selected. **(c)** Meridional cross-sections of Eliassen–Palm flux vectors and divergence (shading). **(d)** Meridional cross-sections of Eliassen–Palm flux vectors and zonal wind (shading). The vectors are plotted for every fifth pressure level.

alignment underscores a connection between stratospheric and tropospheric conditions.

For a more detailed analysis of the vertical propagation of wave activity and its impact on the circulation, the meridional cross-sections of the divergence and vectors of the 3 d averaged EP flux and \bar{u} for the main phases of the 2008 SPV are shown in Fig. 2c and d. Throughout the SPV's displacement and disruption phase, there was a notable enhancement of EP flux convergence and the upward propagation of EP flux vectors. As the EP flux progressively propagated into the stratosphere and northward of 75° N, it resulted in a slowing down of the stratospheric \bar{u} at the pole. From 21 to 23 Febru-

ary, it can be observed that easterly winds are already present in the upper stratosphere, while westerly winds prevail in the middle and lower stratosphere. According to Perlwitz and Harnik (2003) and Kodera et al. (2008), this negative wind shear indicates favorable conditions for the reflection of upward-propagating wave packets. When these wave packets encounter a transition from lower regions (with westerly winds that support the upward propagation of the wave packets) to higher regions (with easterly winds which oppose that propagation), an effective barrier to upward propagation is formed, resulting in the reflection of part of the wave energy. Between 27 and 29 February, the downward propagation of

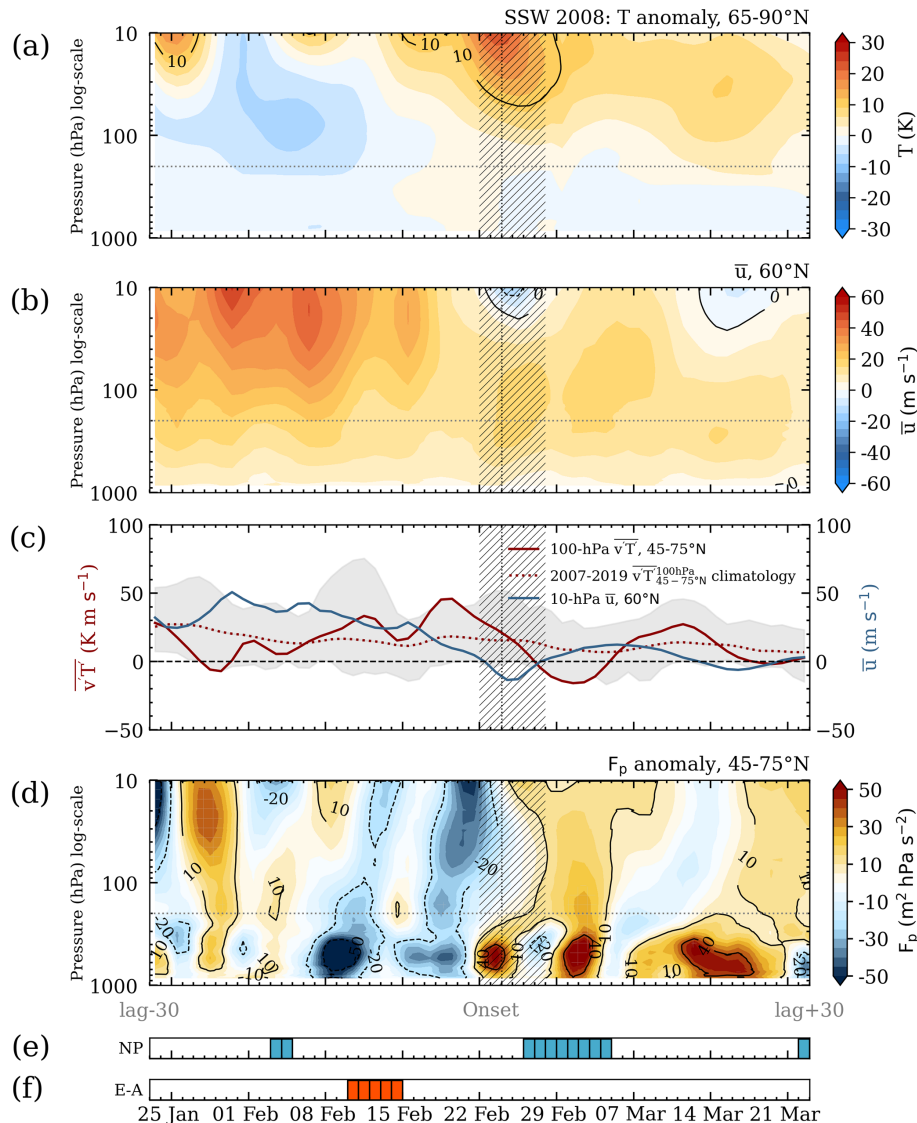


Figure 3. Time–height evolution of (a) the area-weighted temperature anomaly averaged over 65–90° N, (b) the zonal wind at 60° N, and (c) the 100 hPa eddy meridional heat flux averaged over 45–75° N (solid red line), its daily climatology (dotted red line), and the zonal-mean zonal wind at 60° N and 10 hPa (solid blue line). Grey shading covers the region between the daily minimum and maximum of the heat flux for the period 2007–2019. Time–height evolution of (d) the anomaly of the vertical component of the Eliassen–Palm flux averaged over 45–75° N, (e) blocking index for the North Pacific region, and (f) blocking index for the Euro-Atlantic region. The hatched region indicates dates when the zonal-mean zonal wind at 60° N and 10 hPa is negative, and the vertical dotted line indicates the day when the polar (80–90° N) temperature anomaly reaches its maximum, i.e., the start of the SSW recovery phase. The dotted horizontal line indicates 200 hPa (the approximate level of the extratropical tropopause). The time interval shown is ± 30 d from the central date (22 February) of the 2008 SSW.

the EP flux can be observed together with an acceleration of \bar{u} in the stratosphere, indicating that wave reflection is taking place. During those days, it can also be observed that the EP flux divergence in the stratosphere from 10 to 70 hPa is maximized between 70 and 80° N. According to Shaw et al. (2010), the presence of a localized positive EP flux divergence can act as an indicator of a reflecting condition within the atmosphere. A similar EP flux evolution is observed for the 2007 event (Fig. A1c, d).

In addition to the EP flux analysis, to further examine the evidence for the relationship between the downward propagation of wave activity and North Pacific blocking, we analyzed the evolution of the 3D Plumb flux (Fig. B1). Starting from 21–23 February (Fig. B1b), and particularly on 27–29 February 2008 (Fig. B1c), a downward propagation of wave activity between about 250 and 300° E is observed along with a trough centered over 300° E and a positive barotropic geopotential-height anomaly between 150 and

200° E (North Pacific). This is observed together with the eastward tilt of the trough, implying downward propagation of the Rossby waves, aligning with the findings of Kodera et al. (2008). This in turn induced the formation of the North Pacific ridge, which then led to the formation of the North Pacific blocking.

The above analysis finds that the main characteristics of the 2008 and 2007 SSW events are consistent with the characteristics of reflecting SSWs, which in turn is consistent with the findings of Kodera et al. (2008, 2016). On this basis, we classify these SSW events as reflecting events.

4.2 Type II: SSW events from 2009 to 2019

One of the main features of the SSW events that occurred between 2009 and 2019 was the SPV split. The 2010, 2013, 2016, and 2019 events were of mixed type, in which the vortex displaces and then splits (see Figs. 4a, A5a, A7a, and A9a). The 2009 and 2018 SSW events were of the split type (Figs. A3a, A11a). Figure 4a shows the SPV evolution of the 2019 event. A displacement of the vortex towards Eurasia was initiated around mid-December 2018. Beginning on 22 December, the displaced vortex elongated towards the North Atlantic. On 2 January, the vortex reversed and split into two lobes and then continued to split apart until the middle of January.

In the weeks following the vortex displacement in December 2018, the polar-cap temperature anomaly in the stratosphere increased significantly and exhibited a marked downward propagation, extending to approximately 200 hPa (Fig. 5a). The long-lasting deep warming is another commonality of the 2009–2019 SSW events (Figs. A2a, A4a, A6a, A8a, A10a, and A12a). Consistent with the polar-cap temperature variability, the reversal of \bar{u} lasted several weeks in these years, which contrasts with the short duration of the SPV reversal in the 2007–2008 events. The only exception was the 2016 SSW event, during which the SPV did not undergo a recovery phase as it was a final warming event. Nevertheless, this event, with its major SSW characteristics, merits inclusion in our analysis, and it has also been the focus of previous studies such as Manney and Lawrence (2016).

Another interesting feature of these events is the prolonged and gradual wave activity propagation into the stratosphere. The evolution of \bar{u} and $\overline{v'T'}$ in 2019 is shown in Fig. 5c. The $\overline{v'T'}$ peaked on 22 December during the displacement of the vortex, after which \bar{u} began to weaken. Subsequently, as January commenced, the $\overline{v'T'}$ peak underwent a gradual reduction. This was followed by an acceleration of \bar{u} and the eventual recovery of the SPV. Similarly, in 2010, 2013, and 2016, the $\overline{v'T'}$ peaked during the vortex displacement and gradually decreased during \bar{u} reversal (Figs. A6c, A8c, and A10c). In these events, several successive and overlapping peaks in $\overline{v'T'}$ are responsible for the continuous and long-lasting upward wave propagation (about 40 d). In the split events of 2009 and 2018, the peaks in $\overline{v'T'}$ were enhanced

before the vortex split and lasted for 38 and 24 d, respectively (Figs. A4c and A12c). They then gradually decreased until the vortex recovered.

In the time–height view of F_p for the 2019 event (Fig. 5d), the enhanced wave activity pattern first appeared around 4 to 13 December in the troposphere below 300 hPa. This was followed by mildly negative F_p in the whole atmospheric column. Around 23 December, the negative F_p peaked in the stratosphere, extending vertically upward from about 200 hPa. This was preceded by a tropospheric F_p enhancement with a delay of about 8 d. From 25 December, there was another wave activity pattern in the troposphere below 200 hPa, which continued until 1 January. After the reversal of \bar{u} , the troposphere featured a more divergent state, indicating a decrease in wave activity. In the 2009–2018 events, the negative F_p peak in the stratosphere is preceded by a negative F_p peak in the troposphere by a few days before either the SPV displacement (2010, 2013, and 2016) or the SPV split (2009 and 2018 events).

As for the tropospheric response, Euro-Atlantic blocking was observed in the troposphere during the SPV split from late December to mid-January, as shown by the positive 500 hPa geopotential-height anomaly over the Euro-Atlantic in Fig. 4b.

The blocking index captures Euro-Atlantic blocking from 9 to 11 January in Fig. 5f. It can also be observed that the Euro-Atlantic blocking coincided with the configuration of the positive 50 hPa geopotential-height anomaly centered over the North Pole and extended towards the North Atlantic, suggesting a vertical stratosphere–troposphere connection (Fig. 4b). Butler et al. (2020) described that strongly positive stratospheric polar-cap geopotential anomalies or the negative phase of the Northern Annular Mode (NAM) index were observed from the end of December until mid-January 2019 along with North Atlantic blocking. A possible link between this blocking and the SPV configuration in January 2019 is also suggested by Yessimbet et al. (2022b). Similarly, the 2009–2018 SSW events also featured Euro-Atlantic blocking shortly after the SPV split (Figs. A4e–f, A6e–f, A8e–f, A10e–f, and A12e–f), and the geopotential-height configuration resembled a negative AO pattern (Figs. A3b, A5b, A7b, A9b, and A11b).

A closer look at the EP flux during the first week of the recovery phase of the 2019 SSW reveals a continuous upward direction of wave propagation from the troposphere to the stratosphere, as shown in Fig. 4c and d. The large EP flux convergence zone in the stratosphere in early January led to a deceleration of \bar{u} . As the EP flux vectors propagated poleward and upward, the \bar{u} at the pole became easterly and extended downward. To further investigate the relationship between the North Atlantic blocking and the details of wave activity propagation, the 3D Plumb flux evolution and vertically resolved geopotential-height anomalies are shown in Fig. B2. Along with the onset of North Atlantic blocking formation, it can be observed that the wave activity is enhanced outward

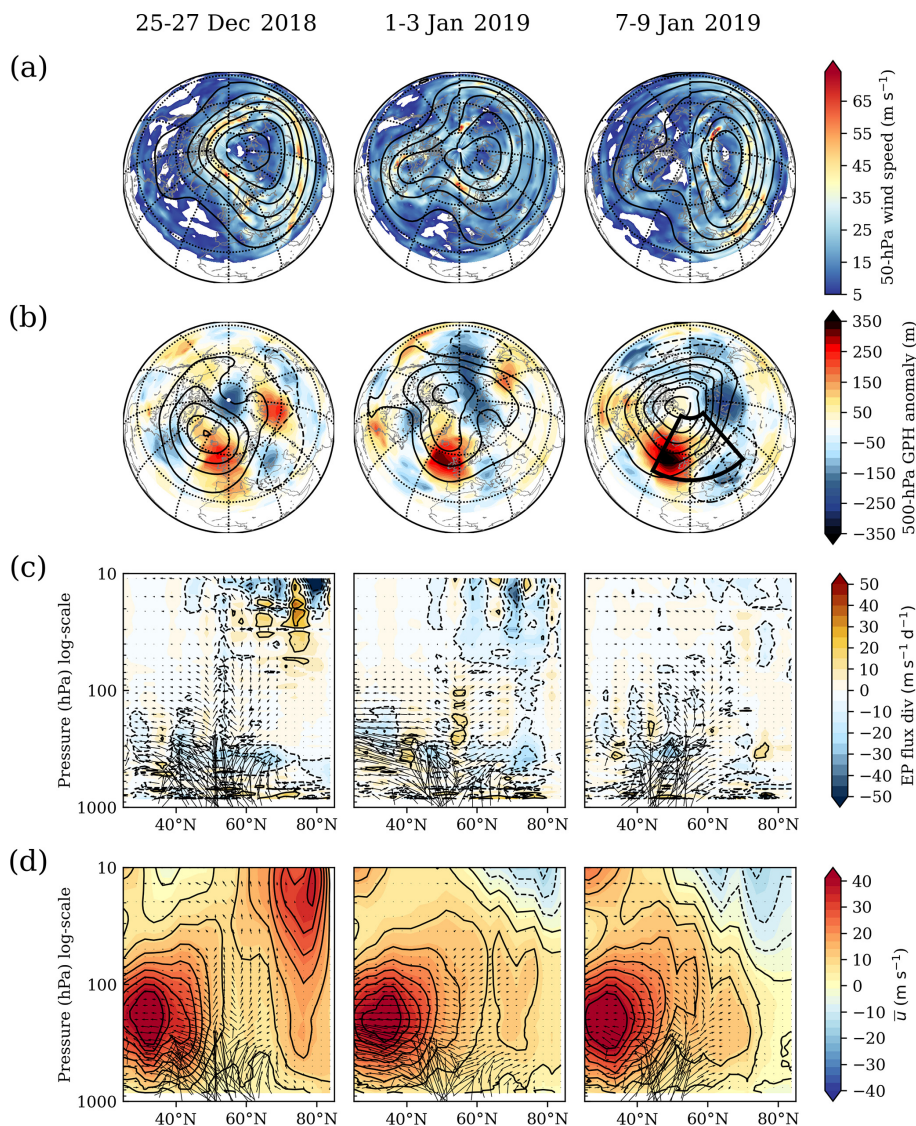


Figure 4. Same as for Fig. 2, but for the 2019 SSW. The 3 d averaged parameters are shown for three dates: during the SPV displacement (left), during the split (center), and after the SPV split (right). The black box indicates the selected Euro-Atlantic blocking region.

from the positive geopotential-height anomalies centered between 50 and 0° W. This suggests that wave packets originating from the North Atlantic block propagate into the stratosphere, thereby contributing to vortex weakening and further SSW development. Overall, the continuous upward propagation of the wave activity (shown by EP flux) into the stratosphere and a deep downward descent of a reversed \bar{u} from the stratosphere into the troposphere during the SSW recovery are also typical for the 2009–2018 events (Figs. A3c–d, A5c–d, A7c–d, A9c–d, and A11c–d).

The characteristics of the SSW events that occurred between 2009 and 2019 align with the description of absorbing SSW events as outlined by Kodera et al. (2016). On this basis, we classify the SSW events from 2009 to 2019 as absorbing.

4.3 Time–height view of the wave activity for 2007–2019 SSW events

Figure 6 displays the time–height evolution of the F_p anomaly averaged over 45–75° N along with the blocking index within a ± 30 d timeframe relative to each of the SSW events between 2007 and 2019.

Before each SSW, there was a pronounced increase in wave activity (indicated by blue shading) in the stratosphere, often extending below 100 hPa. In almost all events, an increase in stratospheric wave activity was preceded by an increase in tropospheric wave activity by several days, indicating upward wave activity propagation. The exception was the 2007 event, during which the stratospheric enhancement occurred without a strong signal of tropospheric wave activity

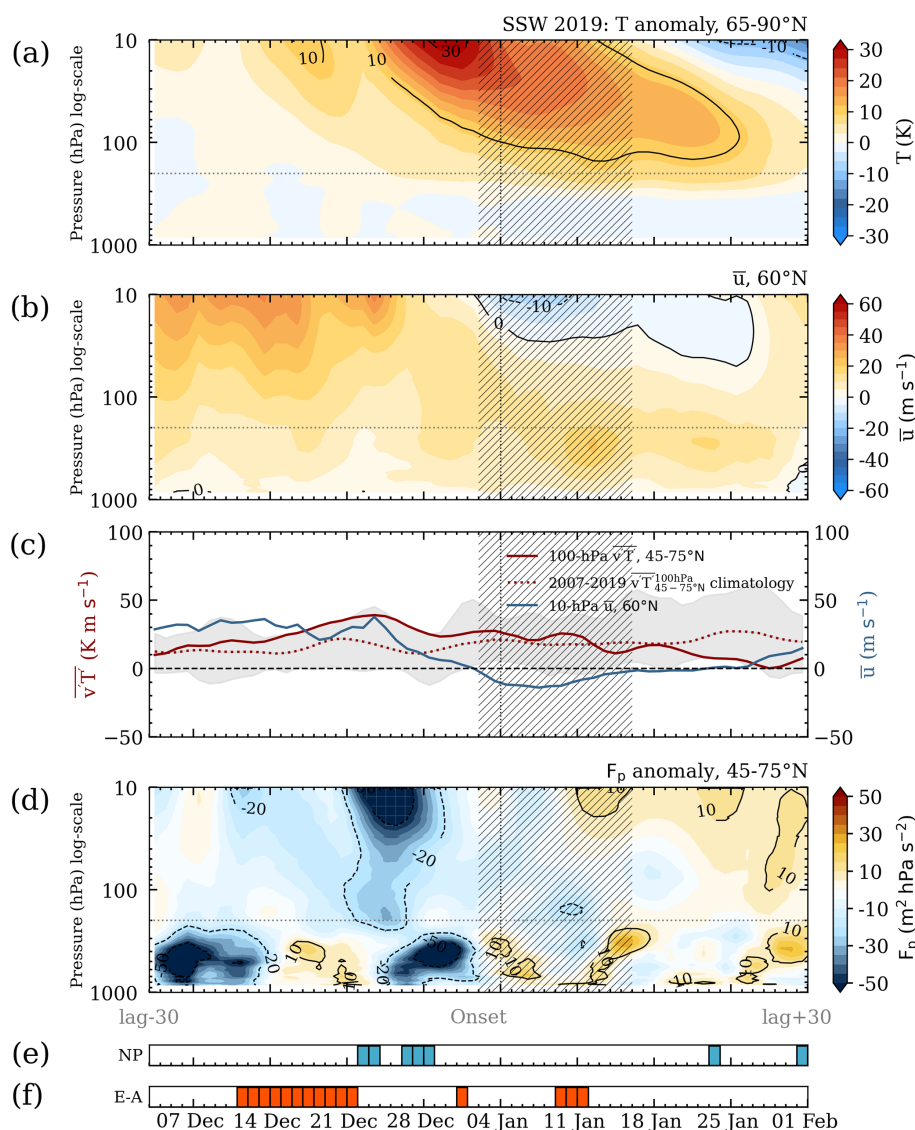


Figure 5. Same as for Fig. 3, but for the 2019 SSW. The time interval is shown for ± 30 d from the central date (2 January).

enhancement preceding it. However, approximately 20 d before that, another notable intensification of wave activity was initially observed in the troposphere and then in the stratosphere above 70 hPa, which suggests the preconditioning of the SPV.

Comparing all individual events, the upward wave propagation signals associated with SSW were less pronounced and shorter in 2007 and 2008, as was the duration of the \bar{u} reversal in these years. In the other six events, the wave activity propagation signals prior to \bar{u} reversal were more pronounced and longer.

The strongest signal of increased wave activity shortly before the SPV split was observed in 2009. For 2010, 2013, and 2019, there was an increase in F_p in the 2 weeks prior to \bar{u} reversal, coinciding with the SPV displacement. At the end of January and beginning of February 2016, there was

an intensification of the F_p , which occurred during a minor SSW event reported by Dörnbrack et al. (2018). In 2018, there were three episodes of F_p enhancement, each separated by an interval of about 2 weeks before the split of the SPV. The first enhancement was continuous throughout the atmospheric column, with a few days lag between the tropospheric and stratospheric anomalies. The second enhancement was observed in the troposphere and then in the stratosphere above 100 hPa, with no vertical continuity between the two regions. These two signals were not sufficient to weaken the vortex and trigger an SSW event. The third F_p anomaly intensification signal was the strongest, with clear signs of upward wave propagation before the SPV split. Interestingly, a closer look at the 2018 SSW event (Fig. A12) reveals that only vertically continuous signals (marked by 100 hPa $\overline{v'T'}$ peaks) coincide with \bar{u} weakening. The same is true for all

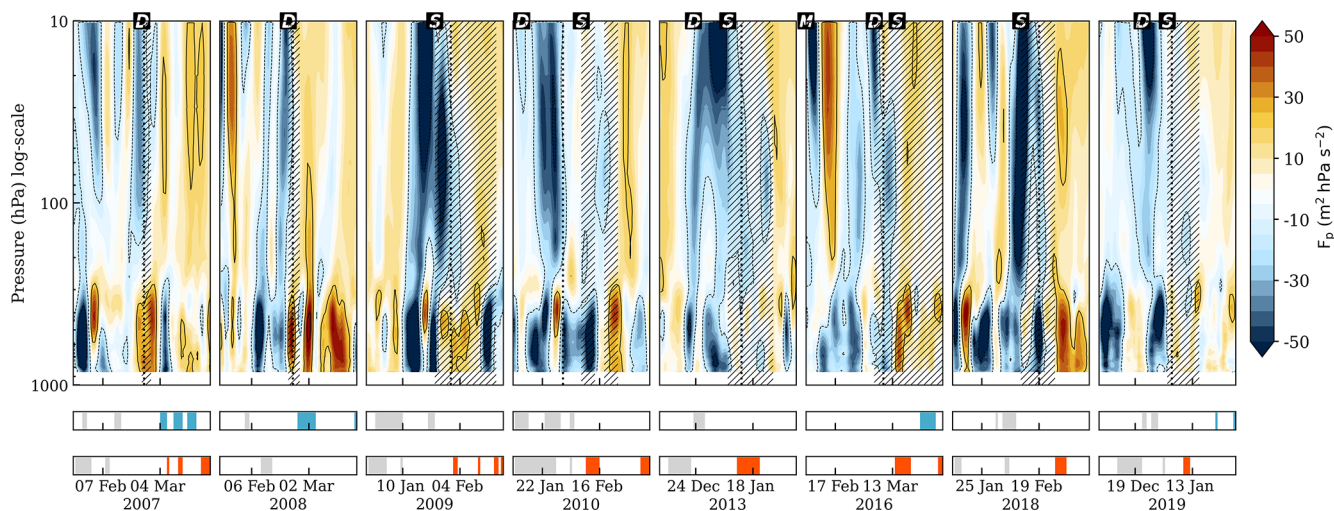


Figure 6. Time–height evolution of the anomaly of the vertical component of the Eliassen–Palm flux ($45\text{--}75^\circ\text{N}$) within a ± 30 d timeframe relative to each of the SSW events from 2007 to 2019. Hatched regions indicate dates when the zonal-mean zonal wind at 60°N and 10 hPa is negative, and the vertical dotted lines indicate the start of the SSW recovery phase. The letters “D” and “S” indicate the approximate start of the SPV displacement and split, respectively. The letter “M” indicates a minor SSW event. The lower panels show the blocking index for the North Pacific (blue) and the blocking index for the Euro-Atlantic region (orange). The blocking events before the SSWs are greyed out.

other SSW events, which may indicate that the propagation or amplification of wave activity in the lower stratosphere (around 100 hPa) is more important for the weakening of SPV than its amplification in the middle and upper stratosphere.

Regarding the blocking events, in both the 2007 and 2008 events, the North Pacific blocking became apparent shortly after the \bar{u} recovery. For the other SSW events, we find that the Euro-Atlantic blocking is observed immediately after the onset of the SSW recovery and during and after (for the 2018 event) the reversal of \bar{u} .

To better understand the differences between the SSW events, we also analyzed the evolution of the zonally averaged polar ($75\text{--}90^\circ\text{N}$) static-stability anomalies (Fig. 7). In the 2009–2019 SSW events, an increase in the static-stability anomaly near 300 hPa can be observed as \bar{u} reverses. This static-stability enhancement indicates a strengthening of the tropopause inversion layer (TIL) in the polar region in the aftermath of SSWs. This observation confirms the findings of Grise et al. (2010), who demonstrated that the magnitude of the TIL is enhanced following SSWs. Also, the case studies of Wargan and Coy (2016) (using reanalyses) and Wang et al. (2016) (using Formosat-3/COSMIC RO measurements) described an enhancement of the static stability in the vicinity of the polar tropopause following the 2009 SSW event.

In our observations, the 2009 and 2013 SSW events had the strongest enhancement of the polar TIL magnitude. We also note the decreasing enhancement of the static stability from the stratosphere to the tropopause level during the onset of the SSWs, which is observed in the static-stability anomalies for the 2009, 2016, 2018, and 2019 SSWs and in

its absolute value for all SSWs (Fig. S4a). This shows that the absorbing SSW events in 2009–2019 had stronger and more prolonged impacts (in terms of thermal heating) on the UTLS and the enhancement of the polar TIL than the reflecting events in 2007 and 2008 did. For the reflecting events, the magnitude of TIL enhancement is much weaker compared to the absorbing events. In 2008, the enhancement of the static-stability anomaly occurred in late March during the final \bar{u} reversal.

5 Discussion and conclusions

The main objective of this study was to characterize the synoptic and dynamic conditions of SSWs and to investigate the link to blocking events from an observational perspective. We used GNSS RO observations for these analyses as the dataset resolves the relevant features to provide information on the stratosphere–troposphere coupling.

Within the timeframe of available RO data spanning from 2007 to 2019, we examined a total of eight major SSW events, including a final SSW event in 2016. To characterize SSWs, we analyzed RO temperature and geopotential-height profiles on isobaric surfaces, which also served as a basis for deriving daily geostrophic winds and quasi-geostrophic EP fluxes. We also computed the blocking index to assess blocking events.

The results showed that the RO data resolve all the main dynamic features of SSWs and troposphere–stratosphere coupling phenomena reasonably well. While the geostrophic-wind speed near the upper-tropospheric subtropical jet and at the SPV level may be slightly underestimated,

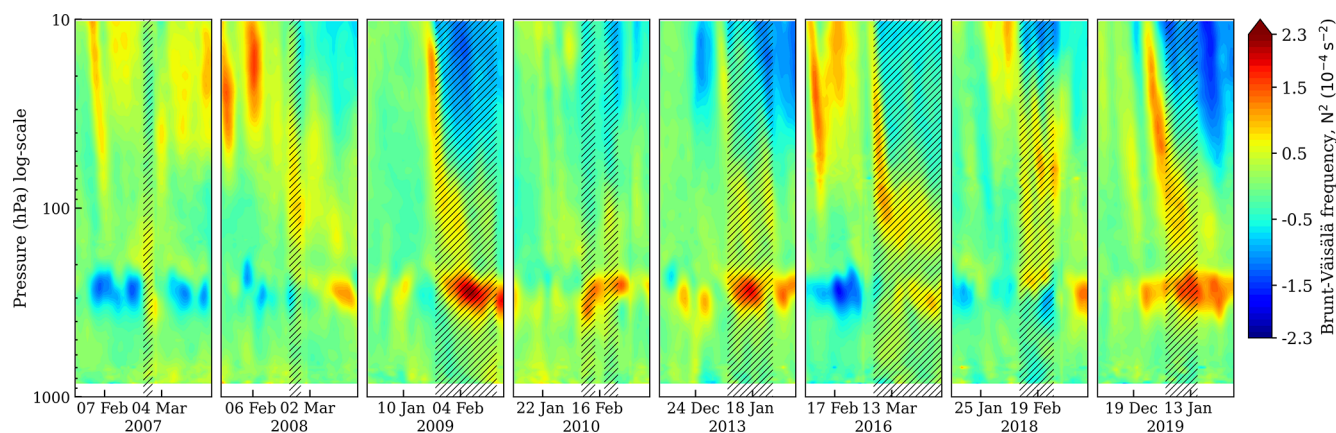


Figure 7. Time–height evolution of the anomalous static stability or the Brunt–Väisälä frequency, N^2 ($75\text{--}90^\circ\text{N}$), within a ± 30 d timeframe relative to each of the SSW events from 2007 to 2019. Hatched regions indicate dates when the zonal-mean zonal wind at 60°N and 10 hPa is negative.

as noted by Scherllin-Pirscher et al. (2014), our study showed that the SPV evolution is well captured. Analyzing the evolution of the SPV, we classified the SSW events into distinct categories – specifically, displacement, split, and mixed-type events. The 2007 and 2008 SSW events were identified as displacement events, while the 2009 and 2018 events were classified as split events and the 2010, 2013, 2016, and 2019 as mixed-type events. A case in point is the 2019 SSW event, which agrees with the findings of Lee and Butler (2020).

Furthermore, our study shows that the key patterns of quasi-geostrophic EP fluxes are well captured and consistent with established theory and the existing literature. Building on the analysis of EP flux evolution, we have classified the SSW events into two categories: reflecting and absorbing events. Thus, the 2007 and 2008 SSW events were categorized as reflecting and the remaining events between 2009 and 2019 as absorbing. For the reflecting SSWs, our observations revealed a short duration of the \bar{u} reversal and a concurrent downward propagation of EP flux during the initial week of the SSW recovery phase. The analysis of the 3D Plumb flux showed that the downward-propagating wave packets induced a trough over eastern Canada and North America and the formation of a ridge over the North Pacific, leading to the onset of North Pacific blocking. On the other hand, absorbing SSW events exhibited a more prolonged \bar{u} reversal and upward propagation of the EP flux. During the recovery phase, these events were accompanied by the formation of blocking in the Euro-Atlantic region and a geopotential-height configuration resembling a negative AO pattern. Enhanced wave activity originating from the North Atlantic blocking was observed to propagate into the stratosphere, thereby potentially contributing to vortex weakening and further SSW development.

These observations agree with the findings of Perlwitz and Harnik (2004), who suggested that there are two types of stratospheric winter conditions, reflective and non-reflective,

which are characterized by different downward dynamic interactions similar to those observed in our study.

Although the reflecting events of 2007 and 2008 were also classified as displacement events and the absorbing events of 2009–2019 as split and mixed events, the relatively limited number of SSW events studied does not allow statistical conclusions to be drawn concerning the consistent alignment of these two classification types. As highlighted in the Introduction, these classifications are rooted in distinct phases of an SSW. The classification based on the polar-vortex geometry is for the mature phase, whereas the classification based on the propagation of planetary-wave activity is for the recovery phase of SSWs.

Nevertheless, we show that reflecting and absorbing SSW events differ in the magnitude of the downward impact (manifested, e.g., in the TIL variability, downward propagation of the easterly wind, and temperature anomalies) and correspond to specific divergent tropospheric responses. Reflecting events connected to vortex displacement are observed to trigger downward wave propagation that induces blocking over the North Pacific region, while absorbing events connected to vortex splitting are associated with blocking over the North Atlantic and upward wave propagation. The magnitude of the downward impact may be one of the factors to consider when addressing the open question of whether displacement or split events trigger different responses in the tropospheric circulation.

Concerning the vertical structure of the quasi-geostrophic EP flux, we observed a consistent pattern of an enhanced upward EP flux (F_p) preceding the \bar{u} reversal in each SSW event. We also observed evidence of upward propagation of wave activity as, prior to each SSW, F_p intensified in the troposphere before intensifying in the stratosphere. This aligns with the hypothesis that an increase in stratospheric wave activity is typically preceded by a burst of wave activity within the troposphere (Polvani and Waugh, 2004). Interestingly,

this contradicts the results of Jucker (2016), who, based on an idealized general circulation model (GCM), did not observe any tropospheric enhancement of wave activity propagating into the stratosphere prior to SSWs. It is worth emphasizing that the peak in wave activity amplification exhibited distinct temporal characteristics for reflecting and absorbing SSW events. Specifically, the amplification peak was shorter for reflecting SSWs than for absorbing events. This suggests the relevance of considering the timescales associated with wave activity pulses. This aspect agrees with the finding of Sjöberg and Birner (2012), who suggested that longer-duration wave activity pulses are more effective at generating SSWs than shorter yet stronger pulses.

In addition, the analysis of polar static-stability anomalies showed that the SSWs are followed by an enhanced polar TIL, which was strongest for the 2009 and 2013 SSW events and weakest for the 2007 and 2008 events. This indicates that the strength of the TIL is influenced by the magnitude of the SSW and its downward impact. Given that TIL enhancement can further influence stratosphere–troposphere coupling and tropospheric circulation, this further emphasizes the distinction between SSW events and their downward influences.

In conclusion, our findings underscore the applicability of GNSS RO for the exploration of atmospheric circulation dynamics. Due to its high vertical resolution, GNSS RO has the potential to study the interplay between tropopause structure and wave activity propagation. A detailed study of the relationship between tropopause structure and wave activity propagation that is relevant to SSW events should be performed in future GNSS RO studies.

Appendix A: SSWs in 2007, 2009, 2010, 2013, 2016, and 2018

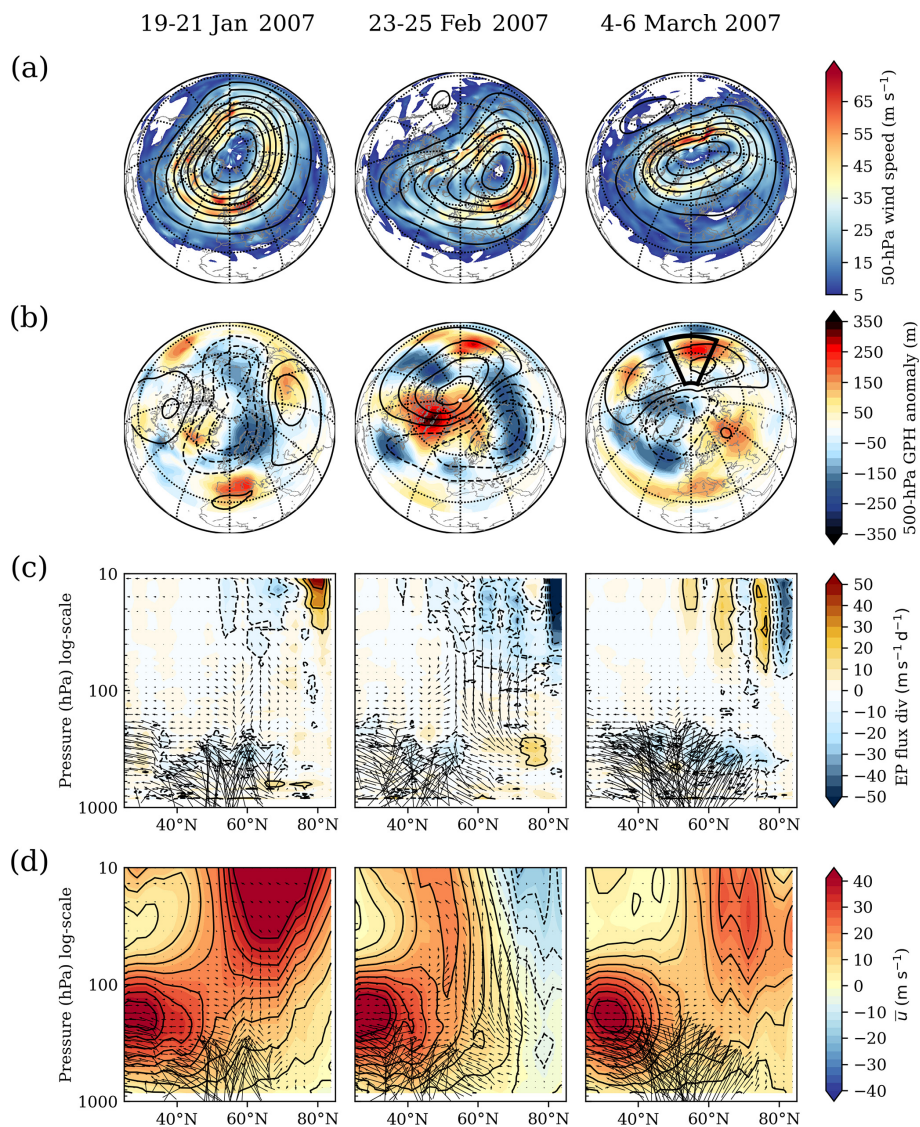


Figure A1. Evolution of the 2007 SSW, as shown by the results for three dates: before the SPV displacement (left), during its displacement (center), and during its recovery (right). **(a)** 50 hPa wind speed (shading) and 50 hPa geopotential height (contours). **(b)** 500 hPa geopotential-height anomaly (shading) and 50 hPa geopotential-height anomaly (contours). The black box indicates the selected North Pacific blocking region. **(c)** Meridional cross-sections of Eliassen–Palm flux vectors and divergence (shading). **(d)** Meridional cross-sections of Eliassen–Palm flux vectors and zonal wind (shading). The vectors are plotted for every fifth pressure level.

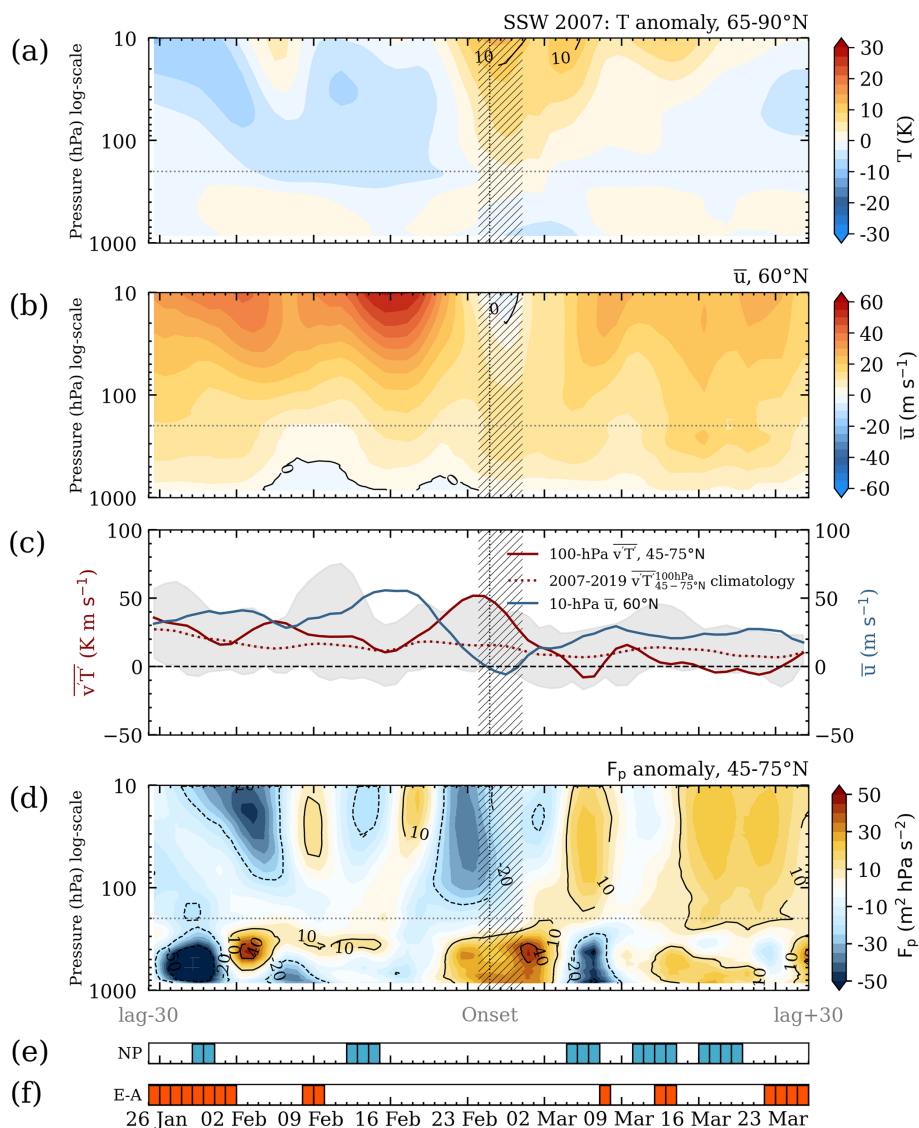


Figure A2. Time–height evolution of (a) the area-weighted temperature anomaly averaged over 65–90° N, (b) the zonal wind at 60° N, and (c) the 100 hPa eddy meridional heat flux averaged over 45–75° N (solid red line), its daily climatology (dotted red line), and the zonal-mean zonal wind at 60° N and 10 hPa (solid blue line). Grey shading covers the region between the daily minimum and maximum of the heat flux for the period 2007–2019. Time–height evolution of (d) the anomaly of the vertical component of the Eliassen–Palm flux averaged over 45–75° N, (e) the blocking index for the North Pacific region, and (f) the blocking index for the Euro-Atlantic region. The hatched region indicates dates when the zonal-mean zonal wind at 60° N and 10 hPa is negative, and the vertical dotted line indicates the day when the polar (80–90° N) temperature anomaly reaches its maximum, i.e., the start of the SSW recovery phase. The dotted horizontal line indicates 200 hPa (the approximate level of the extratropical tropopause). The time interval shown is ± 30 d from the central date (24 February) of the 2007 SSW.

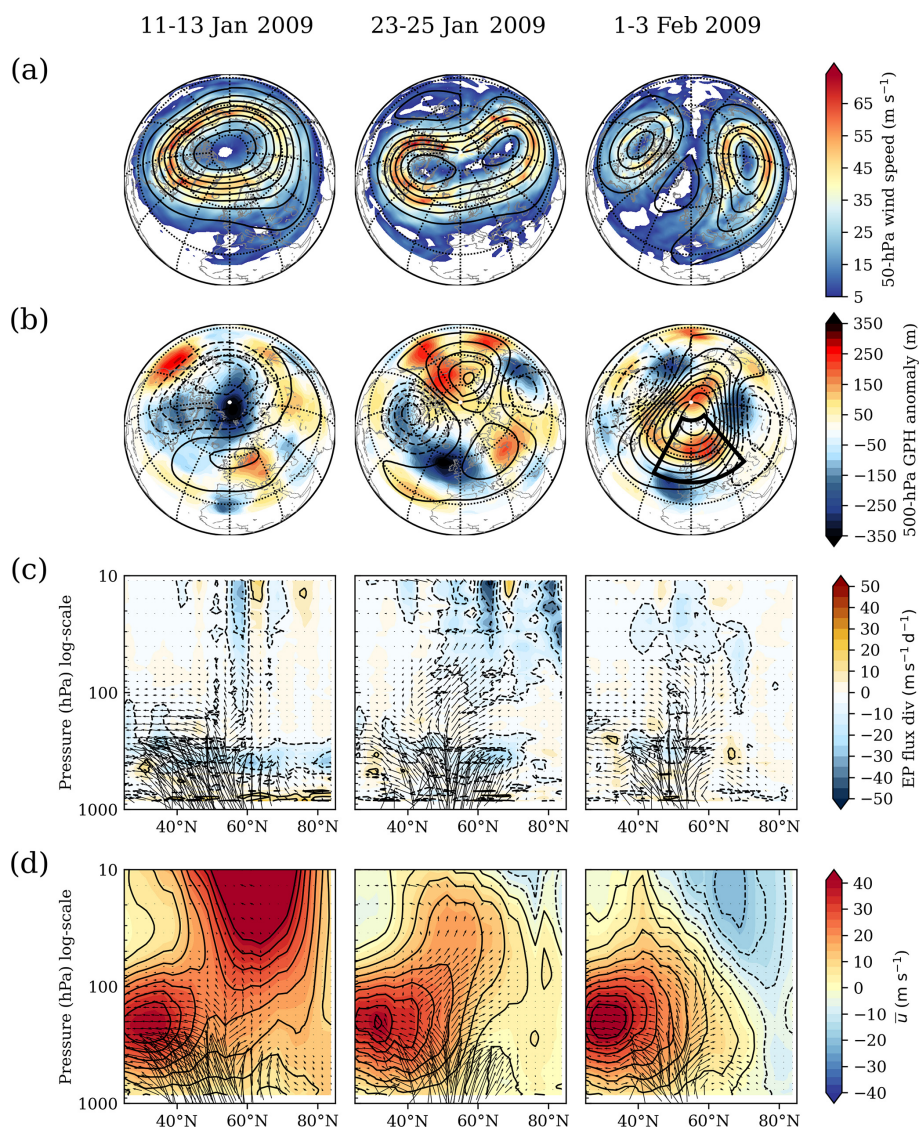


Figure A3. Same as Fig. A1 but for the 2009 SSW. The 3 d averaged parameters are shown for three dates: before the SPV split (left), during the split (center), and after the split (right). The black box indicates the selected Euro-Atlantic blocking region.

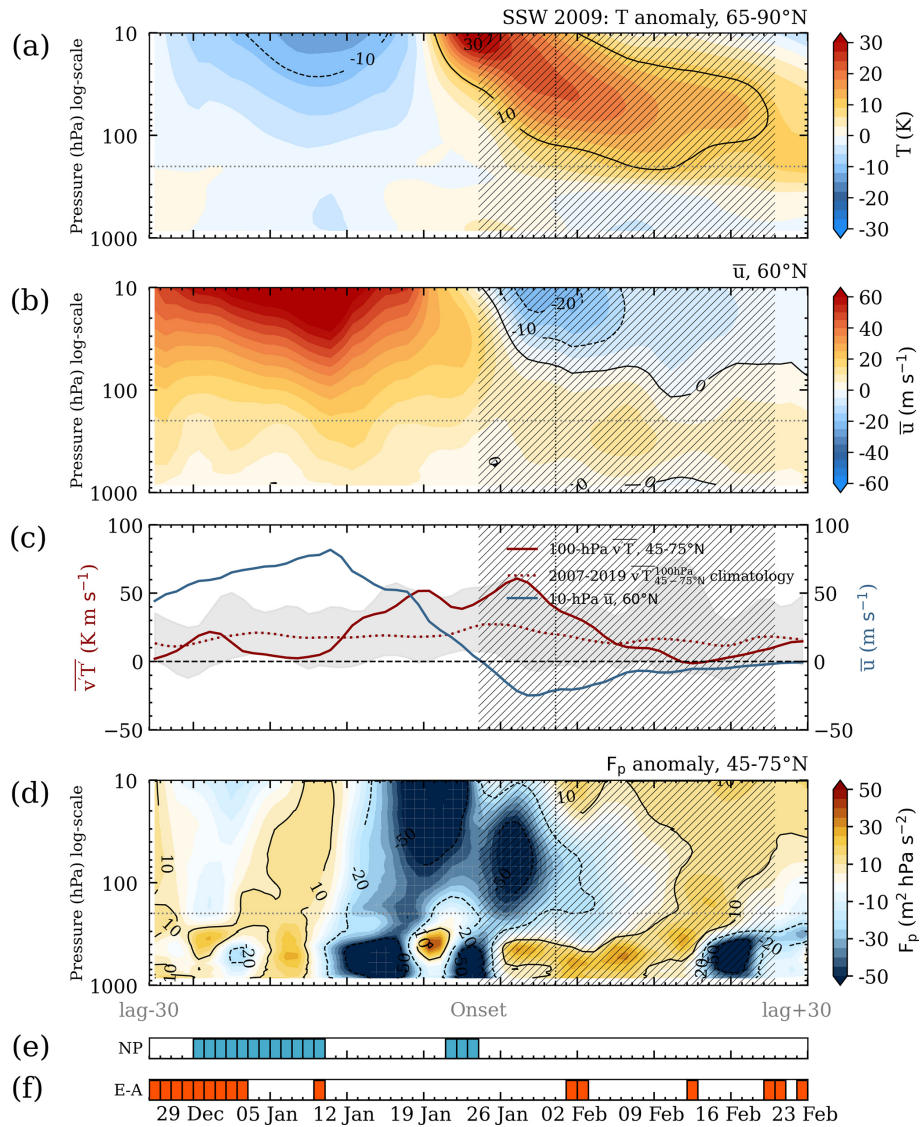


Figure A4. Same as Fig. A2 but for the 2009 SSW. The time interval shown is ± 30 d from the central date (24 January).

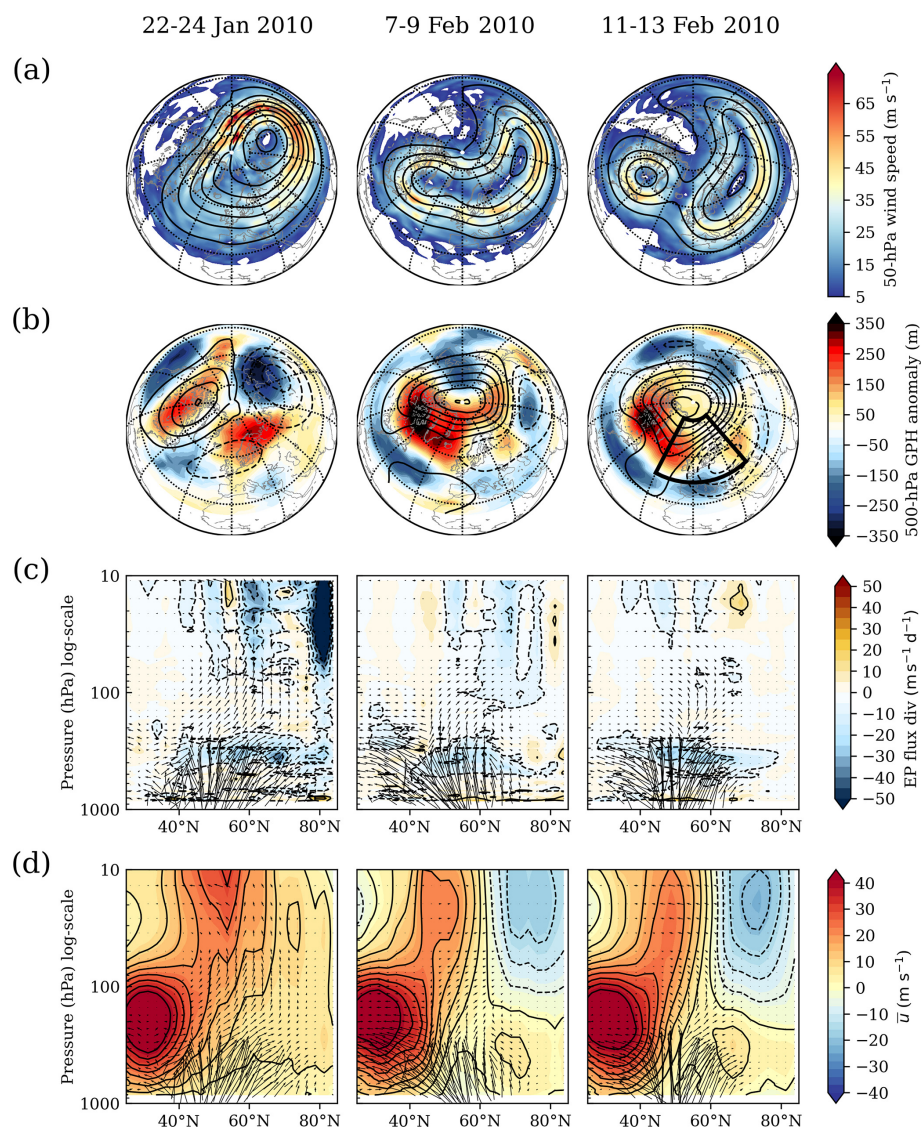


Figure A5. Same as Fig. A1 but for the 2010 SSW. The 3 d averaged parameters are shown for three dates: during the SPV displacement (left), during the split (center), and after the split (right). The black box indicates the defined Euro-Atlantic blocking region.

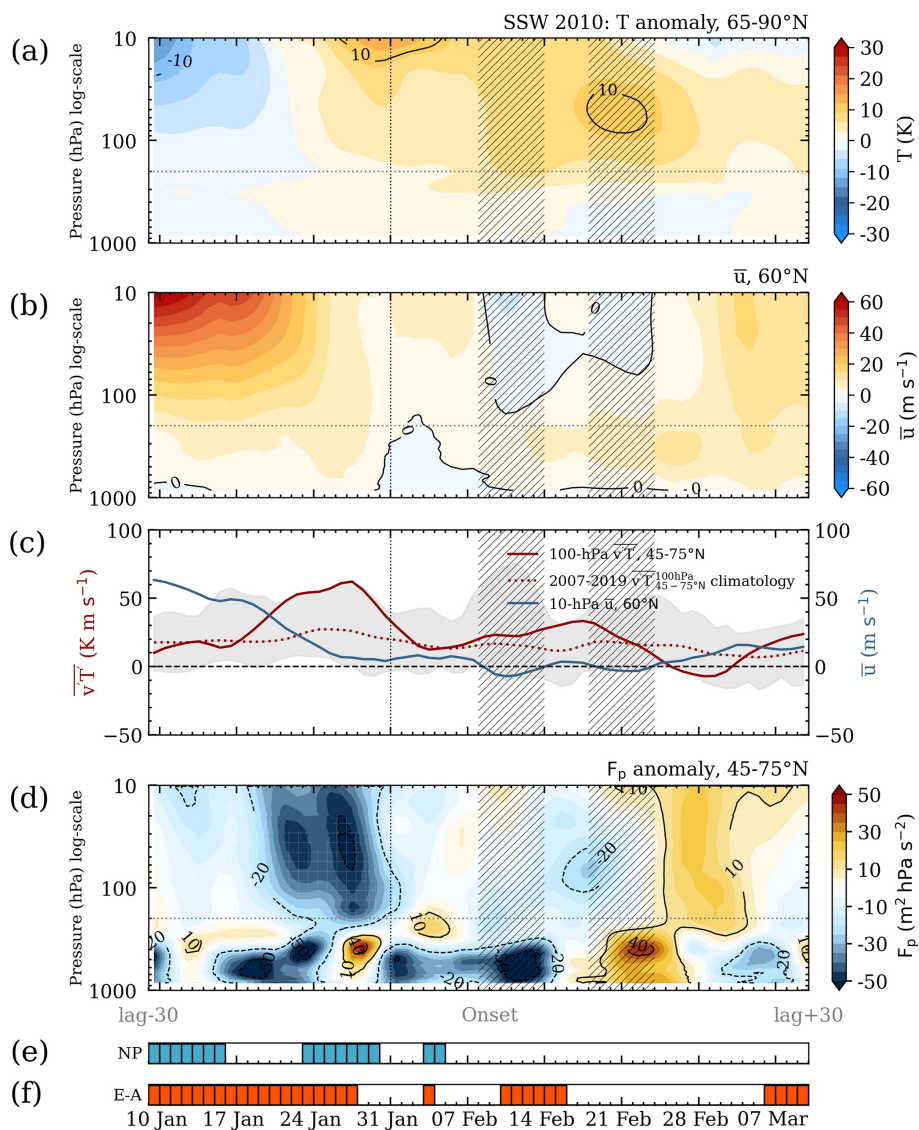


Figure A6. Same as Fig. A2 but for the 2010 SSW. The time interval shown is ± 30 d from the central date (8 February).

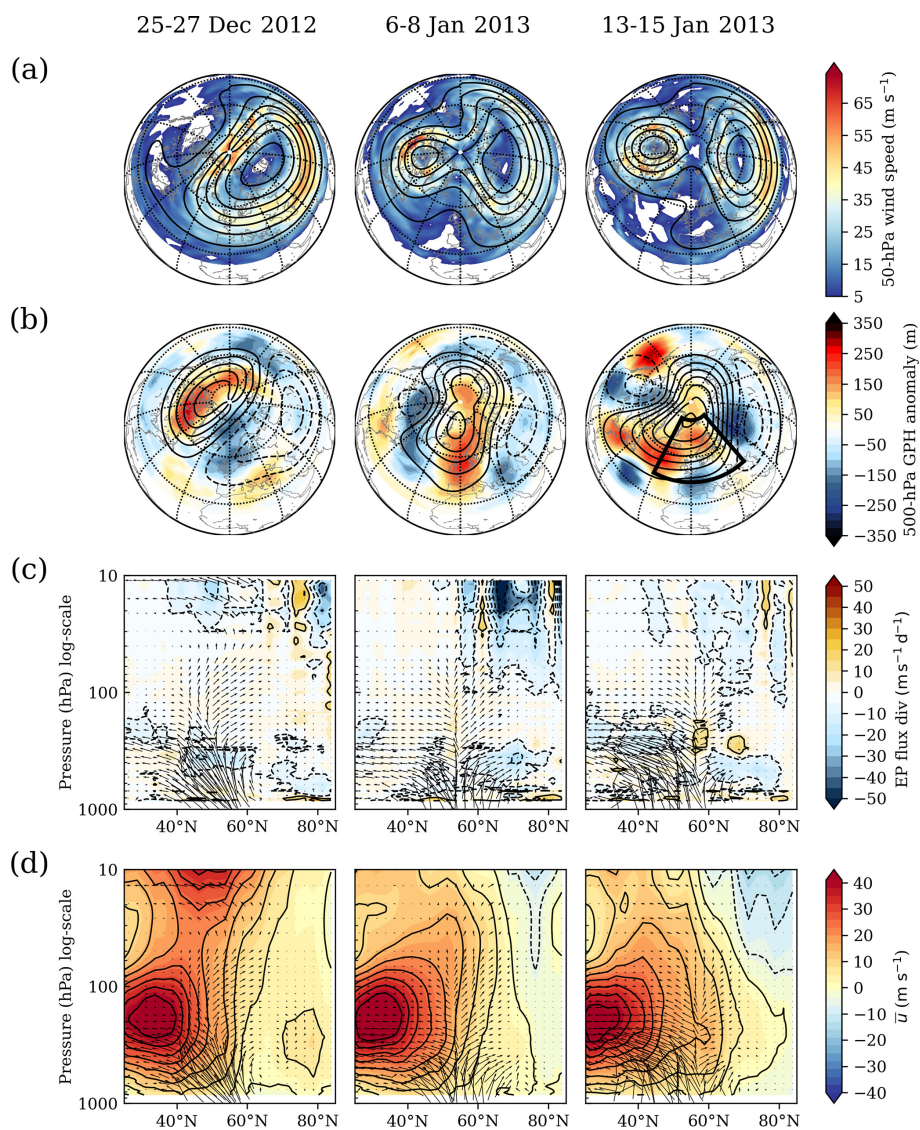


Figure A7. Same as Fig. A1 but for the 2013 SSW. The 3 d averaged parameters are shown for three dates: during the SPV displacement (left), during the split (center), and after the split (right). The black box indicates the defined Euro-Atlantic blocking region.

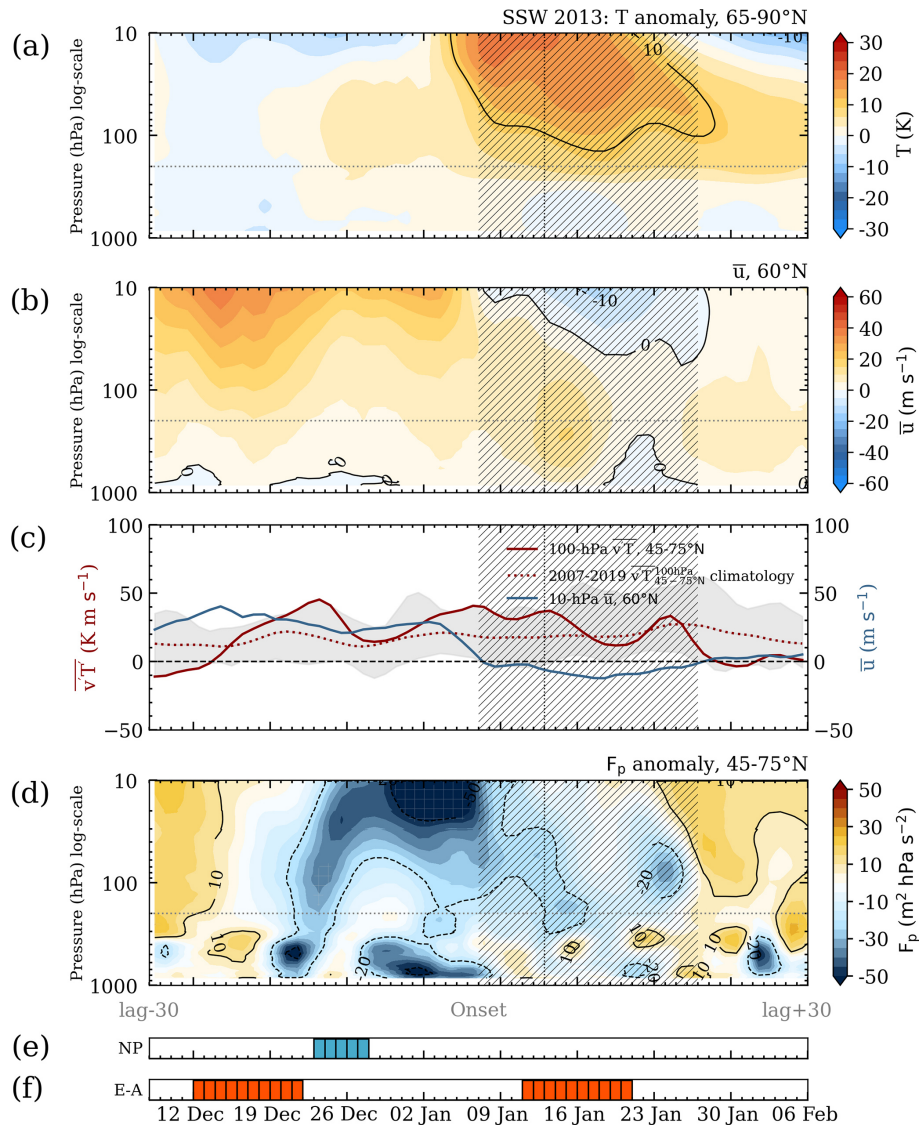


Figure A8. Same as Fig. A2 but for the 2013 SSW. The time interval shown is ± 30 d from the central date (7 January).

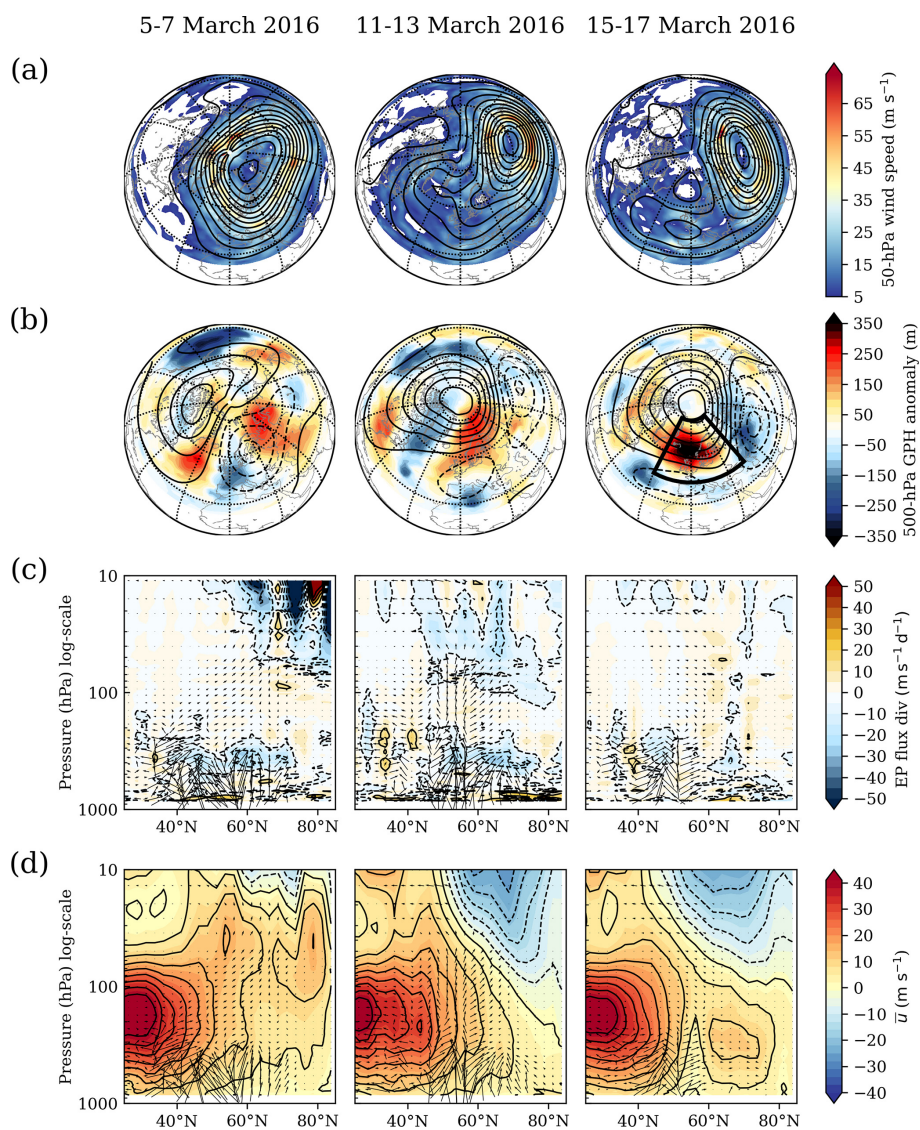


Figure A9. Same as Fig. A1 but for the 2016 SSW. The 3 d averaged parameters are shown for three dates: during the SPV displacement (left), during the split (center), and after the split (right). The black box indicates the defined Euro-Atlantic blocking region.

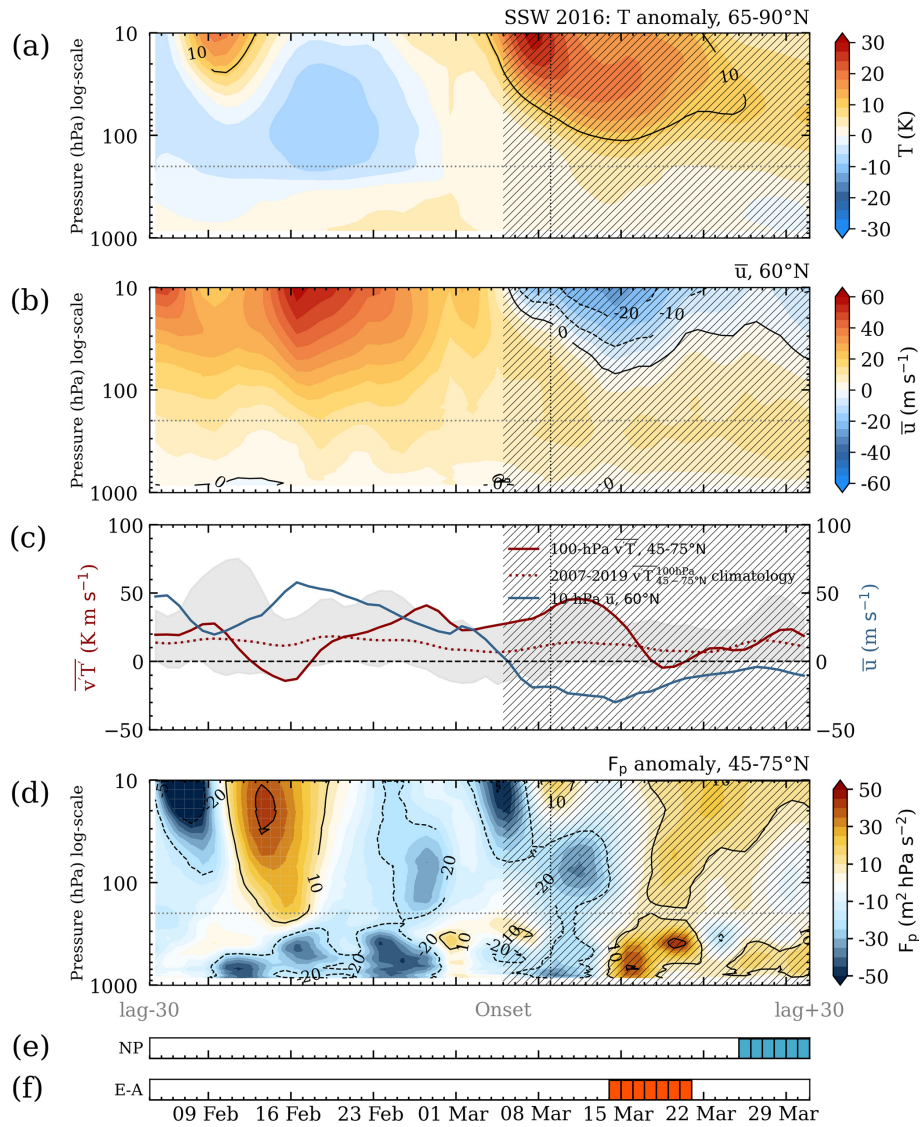


Figure A10. Same as Fig. A2 but for the 2016 SSW. The time interval shown is ± 30 d from the central date (5 March).

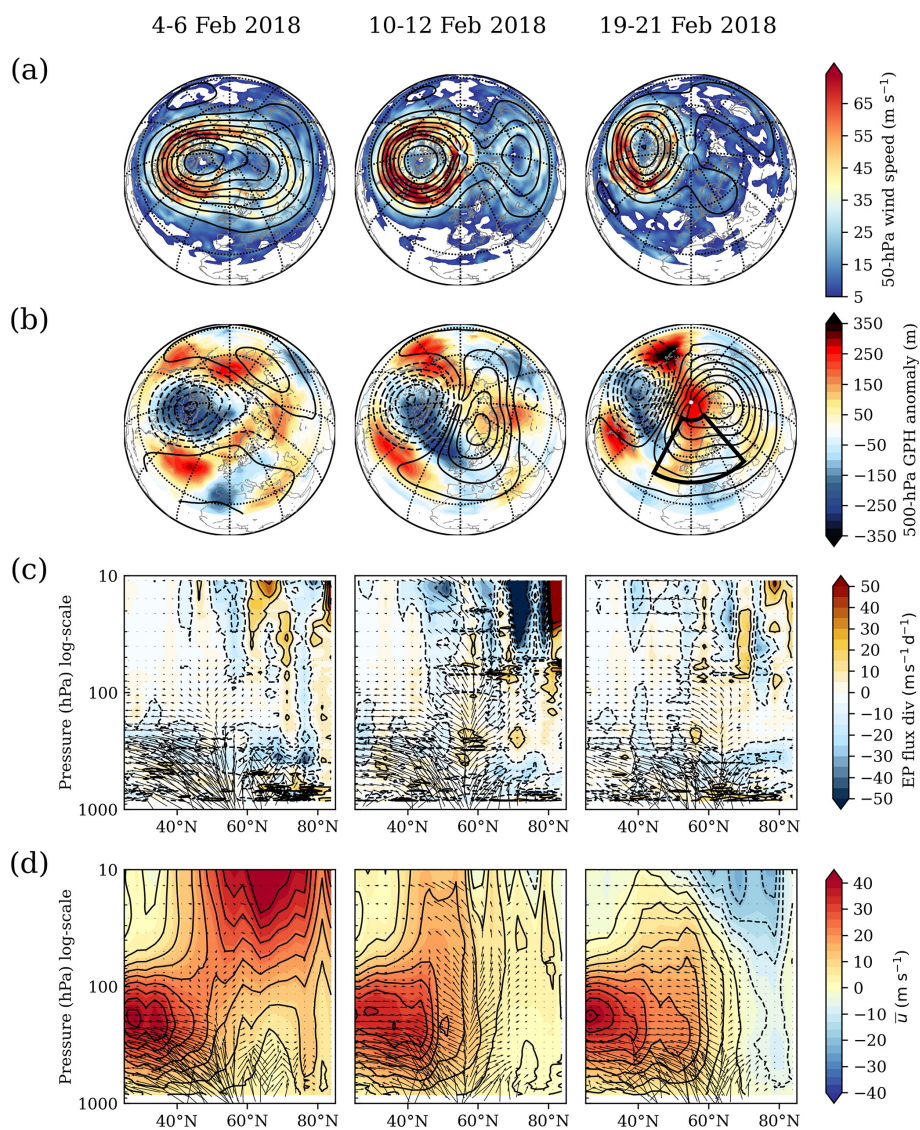


Figure A11. Same as Fig. A1 but for the 2018 SSW. The 3 d averaged parameters are shown for three dates: before the SPV split (left), during the split (center), and after the split (right). The black box indicates the defined Euro-Atlantic blocking region.

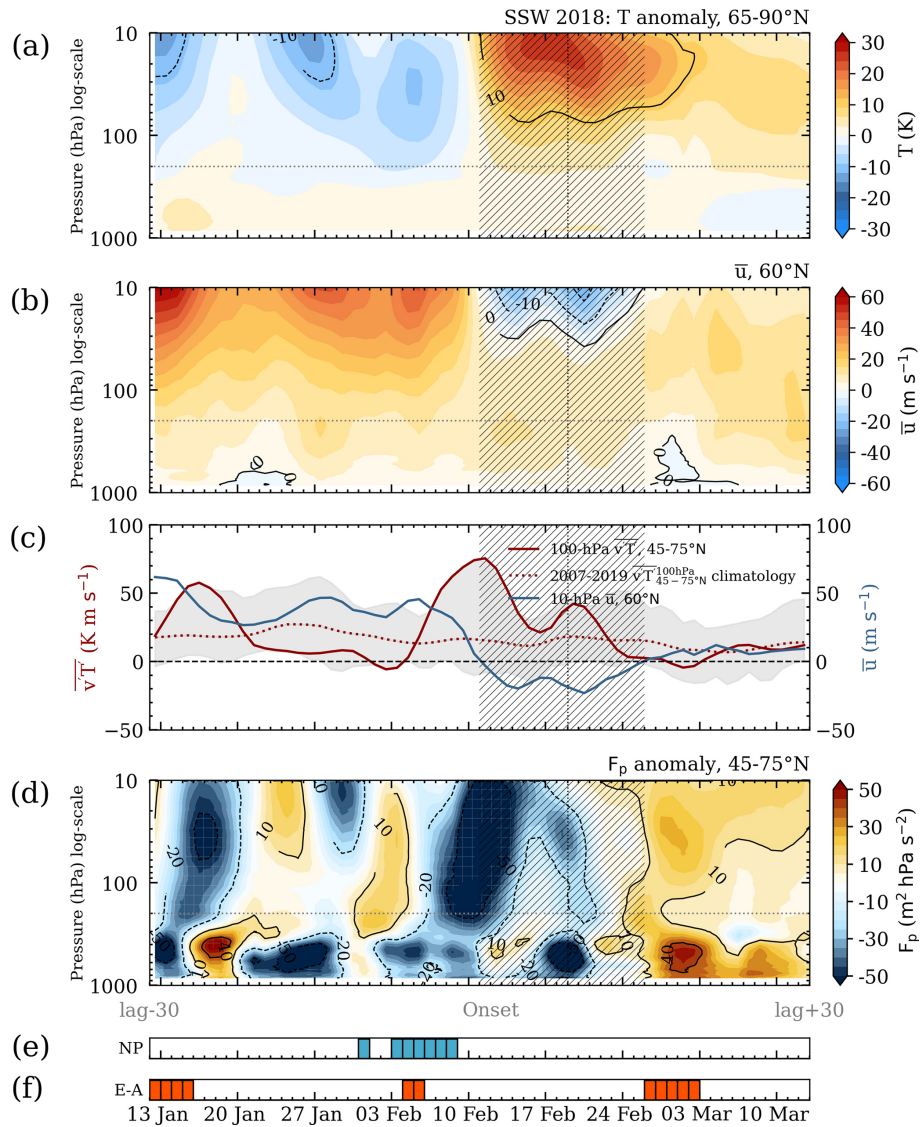


Figure A12. Same as Fig. A2 but for the 2018 SSW. The time interval shown is ± 30 d from the central date (11 February).

Appendix B: Plumb flux

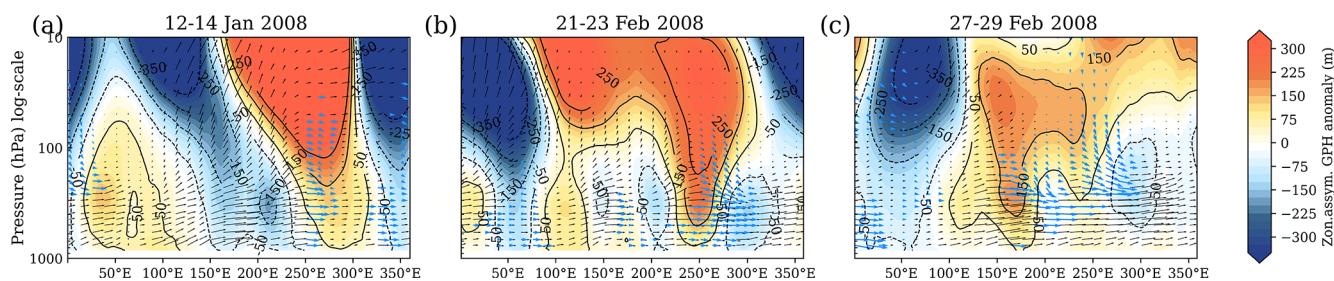


Figure B1. Evolution of the vertical and zonal components of the 3D Plumb flux (arrows) for the 2008 SSW before the SPV displacement (12–14 January), during its displacement (21–23 February), and during its recovery (27–29 February). The vectors are plotted for every fifth longitude and pressure level. Blue vectors denote where the vertical component of the Plumb flux is negative. Shading indicates the zonally asymmetric component of the geopotential-height anomaly.

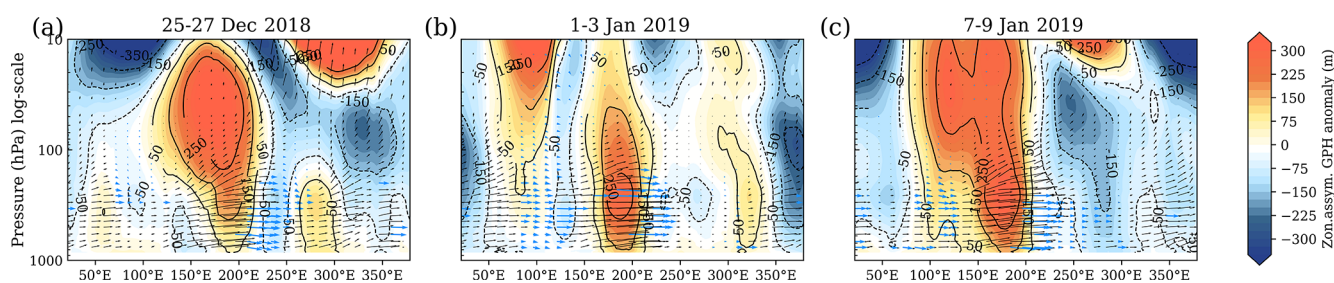


Figure B2. Evolution of the vertical and zonal components of the 3D Plumb flux (arrows) for the 2019 SSW during the SPV displacement (25–27 December 2018), during its split (1–3 January), and after the split (7–9 January). The vectors are plotted for every fifth longitude and pressure level. Blue vectors denote where the vertical component of the Plumb flux is negative. Shading indicates the anomaly of the zonally asymmetric component of the geopotential height.

Data availability. The Wegener Center (WEGC) GNSS RO record OPSv5.6 profiles are available at <https://doi.org/10.25364/WEGC/OPS5.6:2020.1> (EOPAC Team, 2020).

Supplement. The supplement related to this article is available online at: <https://doi.org/10.5194/acp-24-10893-2024-supplement>.

Author contributions. KY contributed to the development of the theory, performed the computational implementation and data analysis, produced all figures, and wrote the first draft of the paper. AKS provided the initial design for this study. FL provided the gridded RO dataset. All authors contributed to the design of the study and figures, the discussion of the results, and the revision of the text. AKS, FL, and AO provided guidance and advice on all aspects of the study.

Competing interests. The contact author has declared that none of the authors has any competing interests.

Disclaimer. Publisher's note: Copernicus Publications remains neutral with regard to jurisdictional claims made in the text, published maps, institutional affiliations, or any other geographical representation in this paper. While Copernicus Publications makes every effort to include appropriate place names, the final responsibility lies with the authors. For the purpose of open access, the author has applied a CC BY public copyright license to any author-accepted manuscript version arising from this submission.

Acknowledgements. We thank the WEGC EOPAC team for providing the OPSv5.6 data profiles. We are grateful to Barbara Scherllin-Pirscher and Lukas Brunner for providing the software used in our study to estimate the geostrophic winds and blocking indices, respectively.

Financial support. This work was funded by the Austrian Science Fund (FWF) under research grant (grant no. W1256) (the doctoral program Climate Change: Uncertainties, Thresholds and Coping Strategies). The authors also acknowledge financial support by the University of Graz.

Review statement. This paper was edited by Peter Haynes and reviewed by three anonymous referees.

References

- Angerer, B., Ladstädter, F., Scherllin-Pirscher, B., Schwärz, M., Steiner, A. K., Foelsche, U., and Kirchengast, G.: Quality aspects of the Wegener Center multi-satellite GPS radio occultation record OPSv5.6, *Atmos. Meas. Tech.*, 10, 4845–4863, <https://doi.org/10.5194/amt-10-4845-2017>, 2017.
- Anthes, R. A.: Exploring Earth's atmosphere with radio occultation: contributions to weather, climate and space weather, *Atmos. Meas. Tech.*, 4, 1077–1103, <https://doi.org/10.5194/amt-4-1077-2011>, 2011.
- Baldwin, M. P. and Dunkerton, T. J.: Propagation of the Arctic Oscillation from the stratosphere to the troposphere, *J. Geophys. Res.*, 104, 30937–30946, <https://doi.org/10.1029/1999JD900445>, 1999.
- Baldwin, M. P. and Dunkerton, T. J.: Stratospheric Harbingers of Anomalous Weather Regimes, *Science*, 294, 581–584, <https://doi.org/10.1126/science.1063315>, 2001.
- Beyerle, G., Schmidt, T., Michalak, G., Heise, S., Wickert, J., and Reigber, C.: GPS radio occultation with GRACE: Atmospheric profiling utilizing the zero difference technique, *Geophys. Res. Lett.*, 32, L13806, <https://doi.org/10.1029/2005GL023109>, 2005.
- Brunner, L.: A new perspective on atmospheric blocking from observations – Detection, analysis, and impacts, PhD thesis, Wegener Center Verlag, Scientific Report No. 76-2018, 2018.
- Brunner, L. and Steiner, A. K.: A global perspective on atmospheric blocking using GPS radio occultation – one decade of observations, *Atmos. Meas. Tech.*, 10, 4727–4745, <https://doi.org/10.5194/amt-10-4727-2017>, 2017.
- Brunner, L., Steiner, A. K., Scherllin-Pirscher, B., and Jury, M. W.: Exploring atmospheric blocking with GPS radio occultation observations, *Atmos. Chem. Phys.*, 16, 4593–4604, <https://doi.org/10.5194/acp-16-4593-2016>, 2016.
- Butler, A. H., Sjöberg, J. P., Seidel, D. J., and Rosenlof, K. H.: A sudden stratospheric warming compendium, *Earth Syst. Sci. Data*, 9, 63–76, <https://doi.org/10.5194/essd-9-63-2017>, 2017.
- Butler, A. H., Lawrence, Z. D., Lee, S. H., Lillo, S. P., and Long, C. S.: Differences between the 2018 and 2019 stratospheric polar vortex split events, *Q. J. Roy. Meteor. Soc.*, 146, 3503–3521, <https://doi.org/10.1002/qj.3858>, 2020.
- Dörnbrack, A., Gisinger, S., Kaifler, N., Portele, T. C., Bramberger, M., Rapp, M., Gerding, M., Faber, J., Žagar, N., and Jelić, D.: Gravity waves excited during a minor sudden stratospheric warming, *Atmos. Chem. Phys.*, 18, 12915–12931, <https://doi.org/10.5194/acp-18-12915-2018>, 2018.
- Edmon Jr., H. J., Hoskins, B. J., and McIntyre, M. E.: Eliassen–Palm cross sections for the troposphere, *J. Atmos. Sci.*, 37, 2600–2616, [https://doi.org/10.1175/1520-0469\(1980\)037<2600:EPCSFT>2.0.CO;2](https://doi.org/10.1175/1520-0469(1980)037<2600:EPCSFT>2.0.CO;2), 1980.
- EOPAC Team: GNSS Radio Occultation Record (OPS 5.6 2001–2019), Wegener Center Data Record, University of Graz, Austria [data set], <https://doi.org/10.25364/WEGC/OPSS.6:2020.1>, 2020.
- Geller, M. A. and Alpert, J. C.: Planetary Wave Coupling between the Troposphere and the Middle Atmosphere as a Possible Sun-Weather Mechanism, *J. Atmos. Sci.*, 37, 1197–1215, [https://doi.org/10.1175/1520-0469\(1980\)037<1197:PWCBTT>2.0.CO;2](https://doi.org/10.1175/1520-0469(1980)037<1197:PWCBTT>2.0.CO;2), 1980.
- Gerber, E. P. and Manzini, E.: The Dynamics and Variability Model Intercomparison Project (DynVarMIP) for CMIP6: assessing the stratosphere–troposphere system, *Geosci. Model Dev.*, 9, 3413–3425, <https://doi.org/10.5194/gmd-9-3413-2016>, 2016.
- Grise, K. M., Thompson, D. W. J., and Birner T.: A Global Survey of Static Stability in the Stratosphere and Upper Troposphere, *J. Climate*, 23, 2275–2292, <https://doi.org/10.1175/2009JCLI3369.1>, 2010.
- Hajj, G. A., Ao, C. O., Iijima, B. A., Kuang, D., Kursinski, E. R., Mannucci, A. J., Meehan, T. K., Romans, L. J., de la Torre Juarez, M., and Yunck, T. P.: CHAMP and SAC-C atmospheric occultation results and intercomparisons, *J. Geophys. Res.-Atmos.*, 109, D06109, <https://doi.org/10.1029/2003JD003909>, 2004.
- Healy, S. B. and Eyre, J. R.: Retrieving temperature, water vapour and surface pressure information from refractive-index profiles derived by radio occultation: A simulation study, *Q. J. Roy. Meteor. Soc.*, 126, 1661–1683, <https://doi.org/10.1002/qj.49712656606>, 2000.
- Healy, S. B., Polichtchouk, I., and Horányi, A.: Monthly and zonally averaged zonal wind information in the equatorial stratosphere provided by GNSS radio occultation, *Q. J. Roy. Meteor. Soc.*, 146, 3612–3621, <https://doi.org/10.1002/qj.3870>, 2020.
- Hines, C. O.: A Possible Mechanism for the Production of Sun-Weather Correlations, *J. Atmos. Sci.*, 31, 589–591, [https://doi.org/10.1175/1520-0469\(1974\)031<0589:APMFTP>2.0.CO;2](https://doi.org/10.1175/1520-0469(1974)031<0589:APMFTP>2.0.CO;2), 1974.
- Jucker, M.: Are Sudden Stratospheric Warmings Generic? Insights from an Idealized GCM, *J. Atmos. Sci.*, 73, 5061–5080, <https://doi.org/10.1175/JAS-D-15-0353.1>, 2016.
- Kodera, K., Mukougawa, H., and Itoh S.: Tropospheric impact of reflected planetary waves from the stratosphere, *Geophys. Res. Lett.*, 35, L16806, <https://doi.org/10.1029/2008GL034575>, 2008.
- Kodera, K., Mukougawa, H., Maury, P., Ueda, M., and Claud, C.: Absorbing and reflecting sudden stratospheric warming events and their relationship with tropospheric circulation, *J. Geophys. Res.-Atmos.*, 121, 80–94, <https://doi.org/10.1002/2015JD023359>, 2016.
- Kursinski, E. R., Hajj, G. A., Hardy, K. R., Romans, L. J., and Schofield, J. T.: Observing tropospheric water vapor by radio occultation using the Global Positioning System, *Geophys. Res. Lett.*, 22, 2365–2368, <https://doi.org/10.1029/95GL02127>, 1995.
- Kursinski, E. R., Hajj, G. A., Bertiger, W. I., Leroy, S. S., Meehan, T. K., Romans, L. J., Schofield, J. T., McCleese, D. J., Melbourne, W. G., Thornton, C. L., Yunck, T. P., Eyre, J. R., and Nagatani, R. N.: Initial Results of Radio Occultation Observations of Earth's Atmosphere Using the Global Positioning System, *Science*, 271, 1107–1110, 1996.
- Lee, S. H. and Butler, A. H.: The 2018–2019 Arctic stratospheric polar vortex, *Weather*, 75, 52–57, <https://doi.org/10.1002/wea.3643>, 2020.
- Leroy, S. S. and Anderson, J. G.: Estimating Eliassen–Palm flux using COSMIC radio occultation, *Geophys. Res. Lett.*, 34, L10810, <https://doi.org/10.1029/2006GL028263>, 2007.
- Luntama, J.-P., Kirchengast, G., Borsche, M., Foelsche, U., Steiner, A., Healy, S. B., von Engeln, A., O'Clérigh, E., and Marquardt, C.: Prospects of the EPS GRAS mission for operational atmo-

- spheric applications, *B. Am. Meteorol. Soc.*, 89, 1863–1875, <https://doi.org/10.1175/2008BAMS2399.1>, 2008.
- Manney, G. L. and Lawrence, Z. D.: The major stratospheric final warming in 2016: dispersal of vortex air and termination of Arctic chemical ozone loss, *Atmos. Chem. Phys.*, 16, 15371–15396, <https://doi.org/10.5194/acp-16-15371-2016>, 2016.
- Matthias, V. and Kretschmer, M.: The influence of stratospheric wave reflection on North American cold spells, *Mon. Weather Rev.*, 148, 1675–1690, <https://doi.org/10.1175/MWR-D-19-0339.1>, 2020.
- Maycock, A. C. and Hitchcock, P.: Do split and displacement sudden stratospheric warmings have different annular mode signatures?, *Geophys. Res. Lett.*, 42, 10943–10951, <https://doi.org/10.1002/2015GL066754>, 2015.
- Messori, G., Kretschmer, M., Lee, S. H., and Wendt, V.: Stratospheric downward wave reflection events modulate North American weather regimes and cold spells, *Weather Clim. Dynam.*, 3, 1215–1236, <https://doi.org/10.5194/wcd-3-1215-2022>, 2022.
- Mitchell, D. M., Gray, L. J., Anstey, J., Baldwin, M. P., and Charlton-Perez, A. J.: The influence of stratospheric vortex displacements and splits on surface climate, *J. Climate*, 26, 2668–2682, <https://doi.org/10.1175/JCLI-D-12-00030.1>, 2013.
- NOAA CSL: Chemistry & Climate Processes: SSWC, <https://csl.noaa.gov/groups/csl8/sswcompendium/majorevents.html>, last access: 1 May 2024.
- NOAA's Physical Sciences Laboratory: <https://psl.noaa.gov/data/epflux/>, last access: 30 November 2023.
- Perlwitz, J. and Harnik, N.: Observational evidence of a stratospheric influence on the troposphere by planetary wave reflection, *J. Climate*, 16, 3011–3026, [https://doi.org/10.1175/1520-0442\(2003\)016<3011:OEOASI>2.0.CO;2](https://doi.org/10.1175/1520-0442(2003)016<3011:OEOASI>2.0.CO;2), 2003.
- Perlwitz, J. and Harnik, N.: Downward coupling between the stratosphere and troposphere: The relative roles of wave and zonal mean processes, *J. Climate*, 17, 4902–4909, <https://doi.org/10.1175/JCLI-3247.1>, 2004.
- Pilch Kedzierski, R., Matthes, K., and Bumke, K.: New insights into Rossby wave packet properties in the extratropical UTLS using GNSS radio occultations, *Atmos. Chem. Phys.*, 20, 11569–11592, <https://doi.org/10.5194/acp-20-11569-2020>, 2020.
- Plumb, R. A.: On the three-dimensional propagation of stationary waves. *J. Atmos. Sci.*, 42, 217–229, [https://doi.org/10.1175/1520-0469\(1985\)042<0217:OTTDPO>2.0.CO;2](https://doi.org/10.1175/1520-0469(1985)042<0217:OTTDPO>2.0.CO;2), 1985.
- Polvani, L. M. and Waugh, D. W.: Upward wave activity flux as a precursor to extreme stratospheric events and subsequent anomalous surface weather regimes, *J. Climate*, 17, 3547–3553, [https://doi.org/10.1175/1520-0442\(2004\)017<3548:UWAFAA>2.0.CO;2](https://doi.org/10.1175/1520-0442(2004)017<3548:UWAFAA>2.0.CO;2), 2004.
- Scherllin-Pirscher, B., Steiner, A. K., and Kirchengast, G.: Deriving dynamics from GPS radio occultation: Three-dimensional wind fields for monitoring the climate, *Geophys. Res. Lett.*, 41, 7367–7374, <https://doi.org/10.1002/2014GL061524>, 2014.
- Scherllin-Pirscher, B., Steiner, A. K., Kirchengast, G., Schwärz, M., and Leroy, S. S.: The power of vertical geolocation of atmospheric profiles from GNSS radio occultation, *J. Geophys. Res.-Atmos.*, 122, 1595–1616, <https://doi.org/10.1002/2016JD025902>, 2017.
- Shaw, T. A., Perlwitz J., and Harnik, N.: Downward wave coupling between the stratosphere and troposphere: The importance of meridional wave guiding and comparison with zonal-mean coupling, *J. Climate*, 23, 6365–6381, <https://doi.org/10.1175/2010JCLI3804.1>, 2010.
- Sjoberg, J. P. and Birner, T.: Transient Tropospheric Forcing of Sudden Stratospheric Warmings, *J. Atmos. Sci.*, 69, 3420–3432, <https://doi.org/10.1175/jas-d-11-0195.1>, 2012.
- Steiner, A. K., Lackner, B. C., Ladstädter, F., Scherllin-Pirscher, B., Foelsche, U., and Kirchengast, G.: GPS radio occultation for climate monitoring and change detection, *Radio Sci.*, 46, RS0D24, <https://doi.org/10.1029/2010RS004614>, 2011.
- Steiner, A. K., Ladstädter, F., Ao, C. O., Gleisner, H., Ho, S.-P., Hunt, D., Schmidt, T., Foelsche, U., Kirchengast, G., Kuo, Y.-H., Lauritsen, K. B., Mannucci, A. J., Nielsen, J. K., Schreiner, W., Schwärz, M., Sokolovskiy, S., Syndergaard, S., and Wickert, J.: Consistency and structural uncertainty of multi-mission GPS radio occultation records, *Atmos. Meas. Tech.*, 13, 2547–2575, <https://doi.org/10.5194/amt-13-2547-2020>, 2020.
- Verkhoglyadova, O. P., Leroy, S. S., and Ao, C. O.: Estimation of winds from GPS radio occultations, *J. Atmos. Ocean. Technol.*, 31, 2451–2461, <https://doi.org/10.1175/JTECH-D-14-00061.1>, 2014.
- Wang, R., Tomikawa, Y., Nakamura, T., Huang, K., Zhang, S., Zhang, Y., Yang, H., and Hu, H.: A mechanism to explain the variations of tropopause and tropopause inversion layer in the Arctic region during a sudden stratospheric warming in 2009, *J. Geophys. Res.-Atmos.*, 121, 11932–11945, <https://doi.org/10.1002/2016JD024958>, 2016.
- Wargan, K. and Coy, L.: Strengthening of the Tropopause Inversion Layer during the 2009 Sudden Stratospheric Warming: A MERRA-2 Study, *J. Atmos. Sci.*, 73, 1871–1887, <https://doi.org/10.1175/JAS-D-15-0333.1>, 2016.
- Wickert, J., Reigber, C., Beyerle, G., König, R., Marquardt, C., Schmidt, T., Grunwaldt, L., Galas, R., Meehan, T. K., Melbourne, W. G., and Hocke, K.: Atmosphere sounding by GPS radio occultation: First results from CHAMP, *Geophys. Res. Lett.*, 28, 3263–3266, <https://doi.org/10.1029/2001GL013117>, 2001.
- Wickert, J., Beyerle, G., König, R., Heise, S., Grunwaldt, L., Michalak, G., Reigber, Ch., and Schmidt, T.: GPS radio occultation with CHAMP and GRACE: A first look at a new and promising satellite configuration for global atmospheric sounding, *Ann. Geophys.*, 23, 653–658, <https://doi.org/10.5194/angeo-23-653-2005>, 2005.
- Yessimbet, K., Shepherd, T. G., Ossó, A. C., and Steiner, A. K.: Pathways of influence between Northern Hemisphere blocking and stratospheric polar vortex variability, *Geophys. Res. Lett.*, 49, e2022GL100895, <https://doi.org/10.1029/2022GL100895>, 2022a.
- Yessimbet, K., Ossó, A., Kaltenberger, R., Magnusson, L., and Steiner, A. K.: Heavy Alpine snowfall in January 2019 connected to atmospheric blocking, *Weather*, 77, 7–15, <https://doi.org/10.1002/wea.4020>, 2022b.